The effect of yttrium additions on the elevated temperature tensile properties and hardness of an advanced iron-nickel-chromium LMFBR cladding and duct alloy

by

Moo Ho Song

A Thesis Submitted to the
Graduate Faculty in Partial Fulfillment of the
Requirements for the Degree of
MASTER OF SCIENCE

Major: Nuclear Engineering

Iowa State University
Ames, Iowa

1981

TABLE OF CONTENTS

I. INTRODUCTION

Rapid increase in energy consumption due to the industrialization of nations and population increases has caused great concern about the depletion of economical energy resources, such as oil, gas and coal, in the foreseeable near future.

As one of the primary alternatives to power from conventional fossil fuel, nuclear power has primarily relied upon light-water cooled and gas-cooled thermal reactors. But thermal reactors use U^{235} as the fissile nuclide, and reserves of uranium are finite. Therefore, in order to extend the uranium reserves, it is imperative to develop and commercialize breeder nuclear reactors which produce more fissile material than they consume. The main breeder approach throughout the world is the Liquid Metal Fast Breeder Reactor (LMFBR).

The basic design of LMFBRs consists of a central core region containing the UO_2-PuO_2 fissile fuel and a surrounding blanket region containing the fertile U^{238} which is converted to fissile Pu^{239}. In comparison with light-water-cooled reactors (LWRs), the LMFBR fuel elements operate at higher temperatures and to higher burnups, and the fuel cladding is subjected to higher neutron fluxes and fluences. To provide better heat transfer, the fuel pins are smaller in diameter; also, the liquid sodium in LMFBRs is a more effective coolant than the water in LWRs. In the Clinch River Breeder Reactor design, the cladding material is 316 stainless steel and the fuel rods are 0.23 inches in diameter. There are 217 fuel rods per assembly contained in a 316 stainless steel duct. There are 198 core assemblies and 150 blanket assemblies. As is pointed out in (1),

major problems are expected to be encountered in the use of 316 stainless steel as the cladding and duct material relating to irradiation swelling, in-reactor creep, and rupture stress. As a result, the generally accepted LMFBR goals of a doubling time (time to double the amount of fuel) of 10-15 years and peak burnup of 150 MWd/kg will not be met.

In order to develop LMFBR cladding and duct alloys with better swelling behavior, resistance to in-reactor creep, and higher rupture strengths, the Energy Research and Development Administration (ERDA, now Department of Energy, DOE) implemented the National Alloy Development Program in 1974, with the objective of developing LMFBR materials with low swelling, good resistance to in-reactor creep, and high rupture strength (1). The sixteen candidate alloys now being screened in this program include eight commercial alloys for LMFBR cladding and duct applications. The commercial alloys and their development alloy counterparts with similar compositions are identified in Table 1.

The LMFBR fuel assembly is expected to be in contact with flowing sodium at temperature ranges from 350°C to 700°C and the transient temperature is as high as 850°C. Historically, most LMFBR reactors used sodium as a reactor coolant. Sodium as a reactor coolant, compared with water or gas, has excellent high-temperature heat transfer and transport properties (2-4). These properties permit high power densities. High thermal efficiencies can be attained because high reactor outlet temperatures obtainable with sodium will lead to highly superheated steam, and, therefore, high Rankine cycle efficiencies. Because of its low vapor pressure and corrosive reaction, the sodium containment system can be thin-walled. The most important consequence of sodium as a reactor coolant is

Table 1. Candidate advanced alloys for LMFBR cladding and duct applications (from Ref. 1)

Alloy class	Candidate commercial alloy	Candidate developmental alloy
Ferritic	HT-9	D57
Austenitic		
Solid solution	316	D9
Precipitation strengthened		
Intermediate nickel	A-286	D21
	M-813	D25
High nickel	Nimonic PE16	D66
	Inconel 706	D68
	Inconel 716	--
	--	D42

a high breeding ratio. This is due to low slowing down power of sodium. A principal reason for selecting sodium for the reactor application instead of other alkali metals is its relatively low cost. Lithium, having high specific heat, costs more than sodium and its relatively low atomic weight might reduce the breeding ratio.

The major effect of exposure of cladding and duct material to high temperature flowing sodium is degradation of mechanical properties due to a loss of surface material and carbon transfer. The corrosion rate is dependent on the temperature and heat flux (1). In connection with sodium purity control, oxygen and hydrogen content in sodium is very important in regard to the corrosion rate of cladding and duct materials. Oxygen and hydrogen control becomes more significant when the alloy contains a high oxygen activity element like vanadium or hydrogen-sensitive element as niobium or zirconium (5,6). Early evaluation stated that carbon transfer in a sodium system, e.g., carbon transfer from ferritic to austenitic steels or from steels to other cladding materials, is controlled by differences in carburizing potential. Carbon transfer is of great concern because a loss of carbon usually reduces strength and pickup of carbon might result in extreme embrittlement of containment or structural materials (1, 2).

The economic feasibility of sodium cooled fast breeder reactors dictates a doubling time of 10-15 years and peak burnups of 100-150 Mwd/kg. To achieve this performance, the fuel assembly will be exposed to a fast neutron fluence of $2\text{-}3\times10^{23}$ n/cm^2 (E > 0.1 MeV), which requires the residence time of fuel assembly in the reactor to be more than 11000 hours at the supposed neutron flux of 5×10^{15}n/cm^2-sec (E > 0.1 MeV).

Past experiences tell us that the most significant phenomena in regard to cladding and duct performance are radiation induced swelling and creep. When high energy neutrons strike the atoms at normal lattice sites, they are displaced and consequently form vacancy-interstitial pairs. In the fast neutron irradiated condition, it is known that vacancies aggregate to form small clusters, and interstitials are absorbed in dislocation loops to form a larger dislocation loop. These vacancy clusters and dislocation loops formed by fast neutron irradiation are called defect clusters. In copper, it had been found that such defect clusters are formed at as low temperatures as $4^{o}K$ (7). In studying radiation induced swelling in pure metals, J. L. Brimhall et al. (8) found that planar vacancy defects form at low temperatures, i.e., at $\gtrsim 0.3\ T_m$ (T_m = absolute melting temperature), and these defects are transformed into three dimensional voids at temperature $\gtrsim 0.3\ T_m$ in most pure metals. In explaining void formation, it is believed that interstitial atoms are preferentially absorbed by dislocation sinks, and, as a result of this preferential absorption, excess numbers of vacancies are available for void formation.

In general, voids are known to occur in the temperature region approximately from $0.3\ T_m$ to $0.55\ T_m$ for pure metals. With increasing temperature, void size increases while number density decreases. At high temperatures, swelling is reduced due to a reduction in the supersaturation of vacancies. With few exceptions, general trends in void swelling for pure metal showed a bell-shaped curve in the temperature ranges from 0.3 $T_m \lesssim T \lesssim 0.55\ T_m$ for constant fast neutron fluences (8). Generally speaking, preferential removal of interstitials by dislocation sinks gives rise

to net growth of voids, but in the case where the dislocation density is extremely high, as in cold worked alloys, dislocations act as efficient sinks both for vacancies and interstitials. Thus, void swelling is decreased in cold worked metals because of decreases in the concentrations of vacancies and interstitials (8). An irradiation study on 25 and 75 percent cold worked 316 stainless steel showed reduced swelling over the temperature range from 370°C to 650°C for a fluence of 3.0×10^{22} n/cm^2 (9-11). For this reason, the Fast Flux Test Facility (FFTF) now being constructed outside Richland, Washington, will use 316 stainless steel cladding and duct material in the 20 percent cold worked condition.

Radiation induced swelling and mechanical strength are strongly dependent on the material composition. Johnston et al. (12) reported that, by increasing the nickel content in austenitic stainless steel, swelling decreased prominantly. In another paper (13), they indicated that swelling further decreased by decreasing chromium content. A recent study on Fe-15% Cr-14% Ni alloys indicated that void nucleation was suppressed in the presence of both Ti and Mo with an increase of Si content (14). In the study on the effects of minor alloying additions on the strength and swelling behavior of Fe-7.5% Cr-20% Ni alloy (equivalent to D11 of the Table 1) using 4 MeV Ni ion bombardment, alloying additions of Ti, C, Nb, Si and Mo were found to be effective in reducing peak swelling. Small amounts of aluminum addition were found to enhance swelling in this alloy (15). It was also found that there occurs various radiation induced, enhanced or modified phases during fast neutron irradiation at elevated temperatures, and much work has been done on the effects of minor elements

and radiation on such phases and on the swelling and mechanical properties of cladding and duct alloys (16).

The effect of irradiation temperature on the mechanical and physical properties of austenitic stainless steels has been reported (17-22). When the steels were tested at temperatures near the irradiation temperature, significantly different damage and corresponding mechanical properties were found in the three different temperature ranges: low temperatures, $T < 0.40T_m$, intermediate temperatures, $0.40\ T_m < T < 0.55\ T_m$, and high temperatures, $T < 0.55\ T_m$ (17). For the low-temperature range, there occurred large increases in yield stress and large decreases in true uniform strain and work hardening exponent (17-19). At intermediate temperatures, where the void swelling is prominent, large increases in yield stress and decreases in ductility took place (20). At high temperatures, increased mobility of radiation induced vacancies and interstititals allowed continuous recovery of defects during irradiation. In this case, the yield stress was unaffected, but the ductility and rupture life were reduced significantly (21, 22). This loss of high temperature ductility is attributed to the helium bubbles formed by (n,α) transmutation reactions during fast neutron irradiation. Table 2 shows approximate cross sections for important elements producing hydrogen and helium as a result of transmutation reactions (17).

Radiation induced creep is defined as the non-elastic deformation which occurs during fast neutron irradiation at temperatures and stresses for which there would be essentially no deformation in the absence of the fast neutron flux. Enhanced creep under the fast neutron irradiation is

Table 2. Transmutation reactions in metals (from Ref. 17)

Nucleus	Reaction	Cross section (millibarns)	Neutron energy associated with cross section
^{14}N	(n,α)	41	Fission
^{10}B	(n,α)	38×10^6	Thermal
	(n,α)	635	Fission
^{56}Fe	(n,α)	0.35	Fission
	(n,p)	0.87	Fission
^{58}Ni	(n,α)	0.5	Fission
	(n,p)	111	Fission

attributed to the enhanced dislocation climb and glide due to the large concentration of vacancies formed upon fast neutron irradiation (1).

Rare earth metals (REMs) include the elements of atomic numbers 57 to 75 (lanthanum to lutetium), plus scandium (atomic number 21) and yttrium (atomic number 39). These elements belong to Group IIIA in the periodic table, and they have similar physical and chemical properties. The applications of REMs in nuclear technology are based on the wide variety of their nuclear properties (23-25). Their neutron absorption cross-sections vary from the millibarn range to the tens of thousands of barns. Another favorable property of some of the REMs in nuclear application is based on high corrosion resistance. Several REMs may serve as in-reactor neutron absorbers. Because of their high neutron absorption cross section and extremely rapid burnup, Gd and Sm are suggested as materials for short-lived core control or shutdown poisons in long-lived cores. Europium, dysprosium, and erbium are slow burnup materials; hence, they may be desirable as control materials. Table 3 shows nuclear properties of REMs in neutron absorber applications. Europium oxide (Eu_2O_3), as an excellent candidate for a neutron absorber in LMFBRs, showed good compatibility with 316 stainless steel at temperatures up to 870°C (26). Satisfactory spectrum-averaged behavior and wide burnable ranges of dysprosium and erbium suggest their application as burnable poisons in various types of reactors.

With its low neutron capture cross section, yttrium also shows a bright prospect for use in nuclear reactors. Yttrium also has a high melting point, low density (27-28), and good corrosion resistance at high

Table 3. Nuclear properties of REMs in neutron absorber application (from Ref. 25)

Element	Primary nuclear Reaction[a]	Thermal neutron absorption cross sections (barns)	Remarks
^{62}Sm	(n,γ) only one isotope	56,000	Of little interest in neutron absorber application
^{63}Eu	(n,γ) chain	4,300	Slow burning material candidate control rod material for LMFBR
^{64}Gd	(n,γ) none-chain	40,000	Too high absorption cross section. Very fast burn up
^{66}Dy	(n,γ) chain	1,100	Desirable for burnable poison as well as control rod material
^{67}Ho	(n,γ) chain	64	Possible flux-suppressor
^{68}Er	(n,γ) only one chain	170	Wide burnable ranges of interest for burnable poison

[a] Eu, Dy and Er have four or five-membered (n,γ) chain, hence they form very desirable control poisoning.

temperature. Table 4 shows some useful physical and mechanical properties of yttrium.

Due to its high thermal stability, yttrium hydride, as a hydrogen carrier, was indicated as a possible high efficiency shield material (24). Early research indicated the possibility of yttrium oxide as a fuel diluent (25). With its expected high melting point and low neutron absorption, Y_2O_3 formed a complete series of solid solutions with UO_2 (26). Yttrium-base dispersions were studied for use in uranium fuels (24, 25).

Direct application of yttrium as a reactor structural material was studied at Ames Laboratory. They proved that yttrium can be used successfully as a structural or container material in a 5% CR-95% U molten fuel reactor when protected from oxidizing atmosphere (24, 25). In England, much work has been done for the high temperature oxidation resistance of yttrium-bearing 20% Cr-25%-Ni Nb-stabilized austenitic steels in a carbon dioxide atmosphere (20-33). Concerning canning materials for the advanced Gas-Cooled Reactor (AGR), small additions of yttrium (0.5-1.0 wt%) were found to provide a significant improvement in oxidation resistance without any loss in other relevant properties such as strength, ductility, creep and strain fatigue resistance. The improvement in oxidation resistance was found to be due to a change in the properties and improved scale adhesion of the oxide layer.

Another possible use of yttrium in nuclear reactor structural applications may be found in the various beneficial effects of REM additions to steels (for reviews, see (34) and (35)). Because of their high reactivity, rare-earth metals combine readily with elements such as O, H, N and S,

Table 4. Physical and mechanical properties of yttrium (from Ref. 27)

Physical properties	
Color	Steel gray
Crystal structure	Close-packed hexagonal up to 1460°C, body-centered cubic above 1460°C
Density at 20°C	4.47 g/cm^3
Melting point	1495 ± 10°C
Thermal conductivity (28°F)	0.035 cal/sq cm/cm/sec/°C
Specific heat at 20°C	0.071 cal/g/°C
Recrystallization temperature	700°C-800°C
Room temperature mechanical properties	
Tensile strength (kpsi)	
as-cast	35.4
annealed	19
Yield strength (kpsi)	
as-cast	28.5
annealed	8
Elongation (%)	
as-cast	9.0
annealed	28
Hardness-Vickers	99
Brinell	30 to 45
Poisson's ratio	0.265
Shear modulus (kpsi)	3700
Modulus of elasticity (kpsi)	9200

although they do not have a high affinity for carbon. Therefore, steels produced with rare-earth additions are likely to be cleaner with reduced sulfide and inclusion content. As a result, the hot workability, high temperature ductility and strength, and oxidation resistance are sometimes improved. Farafanov and coworkers (36) investigated the effects of individual rare-earth additions on the properties of an Fe-20% Ni-15% Cr austenitic stainless steel. In long-term tests, they found that the ductility and time before fracture were increased. They also observed improved scale resistance. In addition, Gryaznov and Paisov (37) studied the effects of cerium additions to an Fe-26% Ni-16% Cr austenitic stainless steel. They observed that cerium additions increased the ductility of the steel, particularly at 950-1200^{o}C in the cast metal. In a later paper, the same authors (38) found that ferro-cerium inhibited the formation of grain boundary carbonitrides, and the hot formability was improved, possibly due to the reduction of surface cracks because of the more uniform distribution of carbonitride inclusions. Additional information on the effects of rare-earth additions on austenitic stainless steels is found in the works of Parsons (39), Etelis et al. (40), Pridantsev et al. (41), Gol'dshtein et al. (42), and Braun and Skok (43).

As mentioned below, it is expected that the generally accepted LMFBR goals of a doubling time of 10-15 years and peak burnup of 150 MWd/kg will not be met with 316 stainless steel as the cladding and duct material (1). The performance capability of 316 stainless steel with regard to swelling, creep rate and rupture stress is compared in Table 5 with the required performance of the cladding and duct material. It is evident that much work needs to be done to reach the required goals. It is possible that some

benefit can be realized as a result of rare-earth additions to the LMFBR developmental alloys. In earlier work at Ames Laboratory, Hopson (44) studied the effect of 0.1% yttrium additions on the ion-induced swelling of two developmental alloys designated as AL1(Fe-26% Ni-9% Cr) and AL2 (Fe-34% Ni-12% Cr), the latter alloy being the same one as employed in the present study. The bombardments were of two types: (1) 4 MeV iron ions and (2) a dual beam of 4 MeV iron ions plus 0.4 MeV helium ions. The results indicated for both alloys and both types of bombardment that the peak swelling was reduced for the yttrium-doped material. In another study, Shah Khan (45) showed that the tensile properties and indentation hardness of alloy AL1 at temperatures up to 800°C were not greatly changed as a result of doping with 0.1% yttrium. The present effort is devoted to a similar investigation of alloy AL2.

Table 5. LMFBR cladding and duct materials-current status and development goals (from Ref. 1)

Performance parameter	Reference 316 stainless steel current status	Advanced alloy Development goals
Swelling, $\Delta V/V$	18 pct at 2.5×10^{23} n/cm^2	5 pct at goal fluence
In reactor creep rate, 45 kg/mm^2 at 650°C	$>6.2 \times 10^{-7}$ hr^{-1}	$<2 \times 10^{-7}$ hr^{-1}
Rupture stress, 20,000 hr at 650°C	36 kg/mm^2	90 kg/mm^2

II. EXPERIMENTAL PROCEDURE

A. Sample Preparation

A heat of a high nickel precipitation strengthened AL2 alloy, investigated in this study, was received from the Hanford Engineering Development Laboratory. This heat was in the form of a bar with dimensions of 1 5/16 inches in diameter and 3 ft in length. Three thin discs with thickness ∿0.1 inches were sliced from the bar for optical metallography, room temperature hardness measurement, and chemical analysis. Six other discs with weights of about 80 gm were also sliced from the as-received bar for arc-melting and further investigation. Table 6 shows the major chemical composition of the heat provided by the manufacturer and by the wet chemistry analysis performed on the slice from the heat.

Six slices were arc-melted and cast into ingots. From these six slices, three slices were doped with 0.1 wt % yttrium and the remainder were arc-melted without yttrium addition ("undoped"). Arc-melted and cast ingots showed finger shapes with elliptical cross section and lengths about 5.5 inches. For the standardization of the procedure, a special cutting scheme was given to the two fingers -- one doped and the other undoped. Samples for chemical analysis and optical metallography were sliced from the different section of the fingers. To see the compositional homogeneity of the fingers, chemical analyses were performed for the samples from the different sections of the fingers. Remaining large pieces were pressed to obtain approximately 10% thickness reductions and then sealed in evacuated quartz tubes. The sealed pieces were given a homogenizing anneal at 1200°C for 10 hours and then cooled in the furnace. After the homogenizing

Table 6. Chemical composition of AL2 alloy (in wt percent)

Element	Chemical composition provided by supplier	Chemical composition from analytical results
Iron	47.3 (by difference)	47.6
Nickel	34.3	34.0
Chromium	11.8	12.3

anneal, other pieces were cut from the original pieces for chemical analysis, optical metallography, room temperature hardness measurement, and electron microprobe analysis.

The other four fingers were not cut before the homogenizing anneal, but pressed to obtain approximately 10% thickness reduction. Then, each finger was sealed in an evacuated quartz tube and then given the homogenizing anneal, as described earlier. After the homogenizing anneal, these four fingers were sliced for chemical analysis and optical metallography.

All the large remaining pieces were pressed once again to obtain from 20 to 25% thickness reduction and then sealed in quartz tubes for the intermediate annealing. Intermediate anneals were performed in a muffle furnace for 1 hour at 1050°C. Then the sealed tubes were removed from the furnace and rapidly cooled in the air.

Rolling was performed at room temperature using a 10" x 14" 2- High STANAT rolling mill. Pieces rolled in the longitudinal direction of the fingers resulted in severe lateral cracks due to uneven amounts of rolling across the rolling surface. For this reason, a transverse rolling direction was employed. A roller speed of 10 feet per minute and thickness reduction from 0.0010 to 0.0025 inches per pass were applied. With the above mentioned rolling condition, the pieces could be rolled to their final thickness of 0.060 inches and 0.030 inches without severe lateral or longitudinal cracking. For each finger and both for 0.030-inch and 0.060-inch sheets, chemical analysis and optical metallography were performed. Composition determination of the second phases shown on the 500X optical metallography was obtained through electron microprobe analysis for both the doped and undoped sheets.

Microhardness specimens were cut directly from the cold rolled 0.060-inch sheet to have a rectangular shape of dimensions 0.45 x 0.65 inches, wrapped in tantalum foil, and then, finally annealed at 1050°C for 1 hour in the vacuum furnace. In this final annealing, 1050°C was obtained within 3 minutes and cooled below 100°C within 5 minutes after anneal in the furnace. Annealed hardness specimens were mounted on carbon blocks and ground and polished to have acceptable specimen surfaces for hardness determinations. Special care was given during the grinding and polishing to keep an even thickness to the specimens. After polishing, hardness specimens were removed from the carbon block and used for hardness tests.

The 0.030-inch sheet samples were sealed in evacuated quartz tubes and annealed at 1050°C for 1 hour and then cooled to room temperature in air. To prepare the tensile specimens, annealed 0.030-inch sheet samples were sheared longitudinally parallel to the rolling direction. These 0.195-inch-wide sheared strips were cut to have a rectangular dimension of 1.6" x 0.195 inches, and then stacked in a specially designed fixture. Stacked plates were fastened using screws installed on the one side of the fixtures. Figure 1 shows the layout of the tensile specimen grinding fixture. The tensile specimen grinding fixture, with 1.6 x 0.195 inch plates stacked and fastened within its groove, was fixed on a grinder table and ground by moving a disc grinder to the designed dimensions of the tensile specimen, as shown in Figure 2. After grinding, the tensile specimens were cleaned with acetone and methanol, wrapped in tantalum foil, and, finally annealed in the vacuum furnace for 1 hour at 1050°C (i.e., receiving the same heating cycle as that of the microhardness specimens).

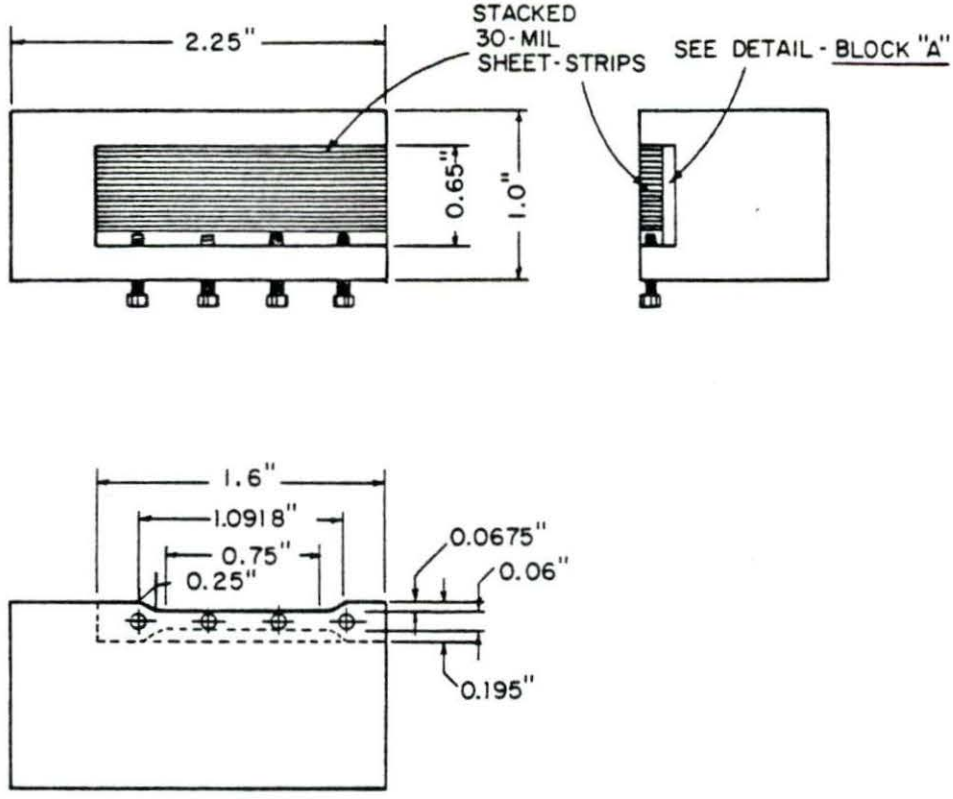

DETAIL - BLOCK "A"

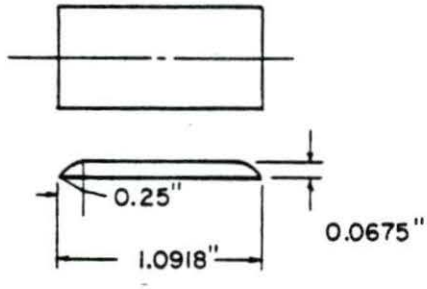

Figure 1. Schematic diagram of the tensile specimen grinding fixture.

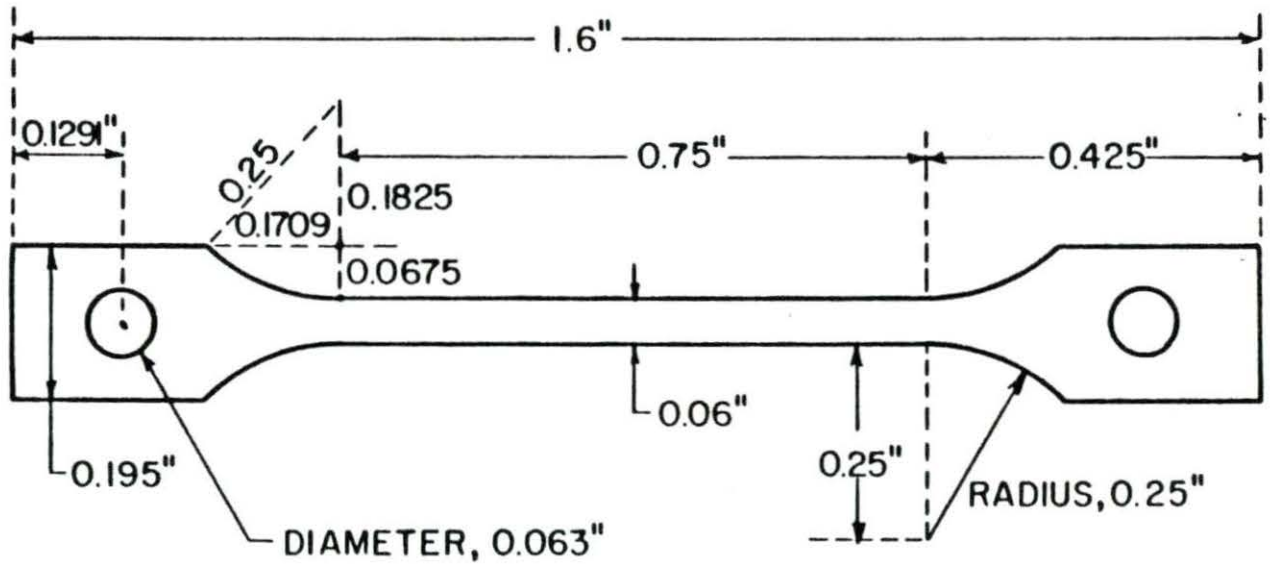

Figure 2. Dimensional view of the 30 mil thick sheet tensile specimen

B. Tensile Test Apparatus

Elevated temperature tensile tests were performed on the model TT-C-L Instron machine according to the requirements of ASTM specifications E4-72, E8-69, E21-70 and E-151 (46-49). The high temperature tensile test assembly used in this experiment consists of a screw-driven Instron machine and a control console, a pull-rod assembly and vacuum jacket, specimen heating furnace and a temperature control system. The Instron machine is operated by the moving crosshead and load weighing system. The moving crosshead to which the lower pull-rod is attached is operated by the two vertical drive screws from a unique positional servo drive. The chart of the recorder from which the tensile properties are determined operates synchronously with respect to the speed of crosshead at a wide variety of speed ratios. The load weighing system is comprised of an interchangeable load cell. All through the tests, a load cell of type "F" was used. This cell has load ranges of 200, 500, 1,000, 5,000 and 10,000 pounds for normal sensitivity. As shown in Figure 3, the upper pull-rod is attached to the load cell by means of a flexible coupling, and, as mentioned earlier, the lower pull-rod is attached to the mount located on the center of the moving crosshead. Both attachments of the pull-rods use pins and engaging slots.

The pull-rod assembly consists of an upper pull-rod, a lower pull-rod, and pin-type specimen grips. The specimen grips are installed between the pull-rods by the end-threaded pin and slots. Pull-rods and specimen grip are made of high temperature material to have a tensile strength exceeding 1,500 pounds at 2200 F. The pull-rod vacuum jacket is furnished

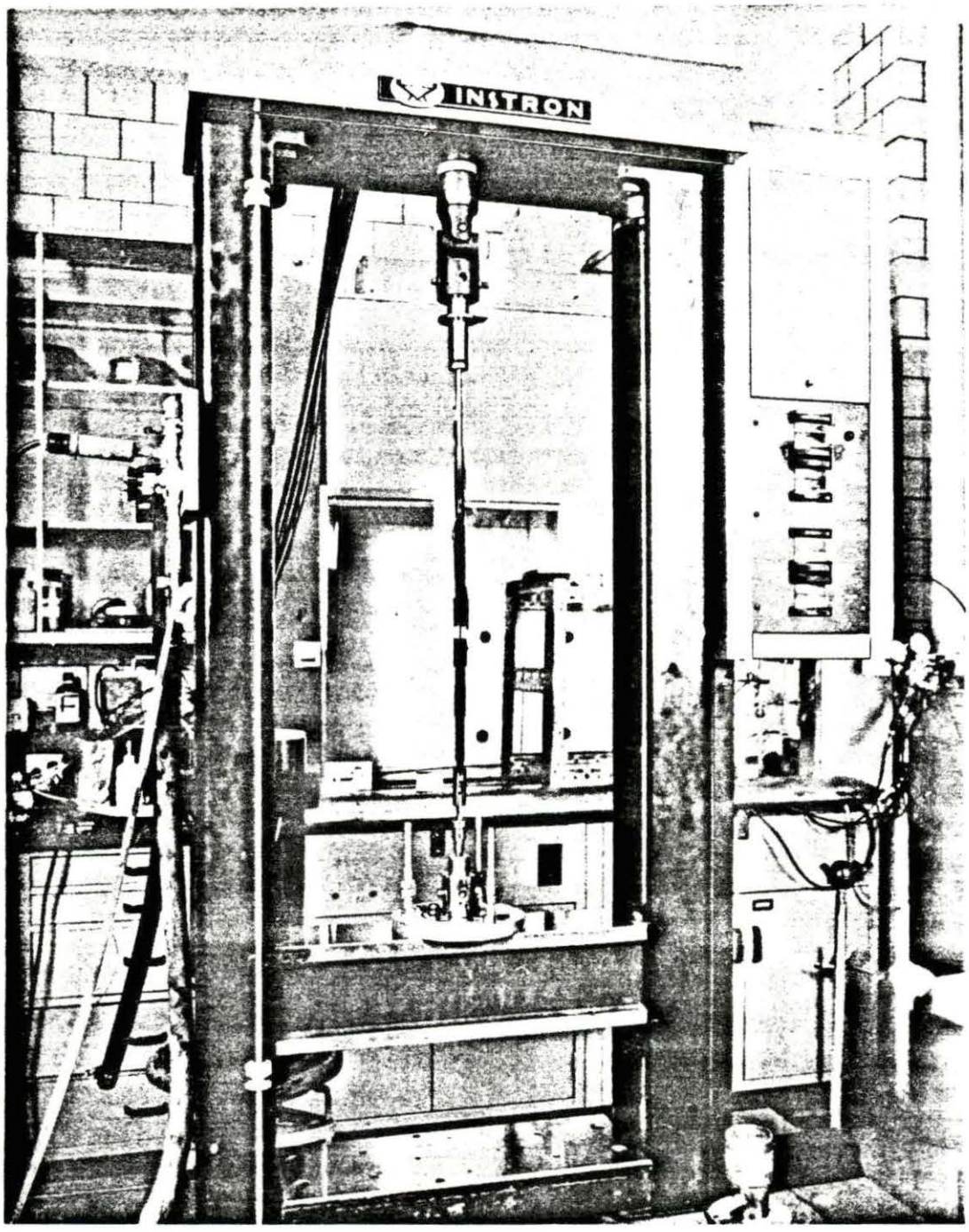

Figure 3. Load frame and the specimen pull-rod assembly

with a vacuum shut-off valve and holds the bottom and top O-ring cooler. Both O-ring coolers are operated by flowing compressed air. The purpose of the top O-ring cooler is to prevent the O-ring temperature and load cell temperature from exceeding designed limits. The bottom O-ring cooler is installed to prevent the hardening of the O-ring and degradation of vacuum at high temperature operation. The vacuum jacket shut-off valve is connected to both a mechanical pump and an argon gas cylinder to permit the testing in an argon atmosphere. An installed pull-rod vacuum jacket, with pull-rod assembly within it, is shown in Figure 4.

Specimen heating is done by a cylinder-type resistance furnace mounted at the center of the moving crosshead. The furnace uses Kanthal windings around a refractory tube and has three zones: top, center and bottom. The furnace temperature is controlled by the ON-OFF type controller which uses input EMF from the control thermocouple (Pt-Pt 13% Rh) installed near the windings and which provides separate variac control for the three zones of the furnace. The furnace and controller system is designed to perform tensile tests from room temperature up to 1200^{o}C in vacuum or inert gas atmosphere. Whole setting of pull-rod assembly and vacuum jacket, and specimen heating furnace are shown in Figure 5.

Specimen temperature monitoring thermocouple (chromel-alumel) is installed at 3-5 mm apart from the center of the specimen gauge section. Another chromel-alumel thermocouple is imbedded near the control thermocouple. Both specimen temperature and furnace temperature are recorded by the Bristol 12-channel temperature recorder. The specimen temperature is also displayed by a digital thermometer.

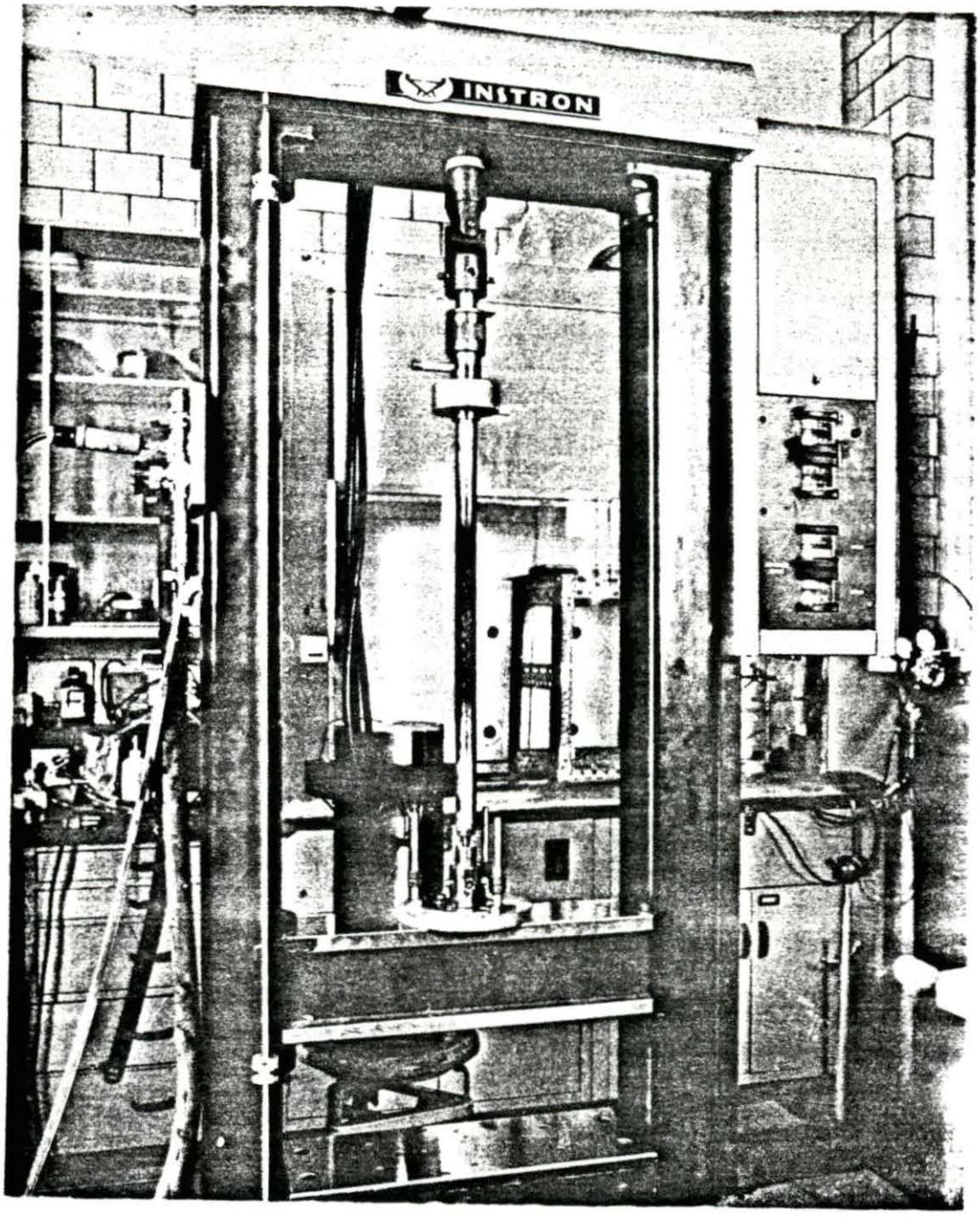

Figure 4. Load frame and pull-rod vacuum jacket with specimen pull-rod inside

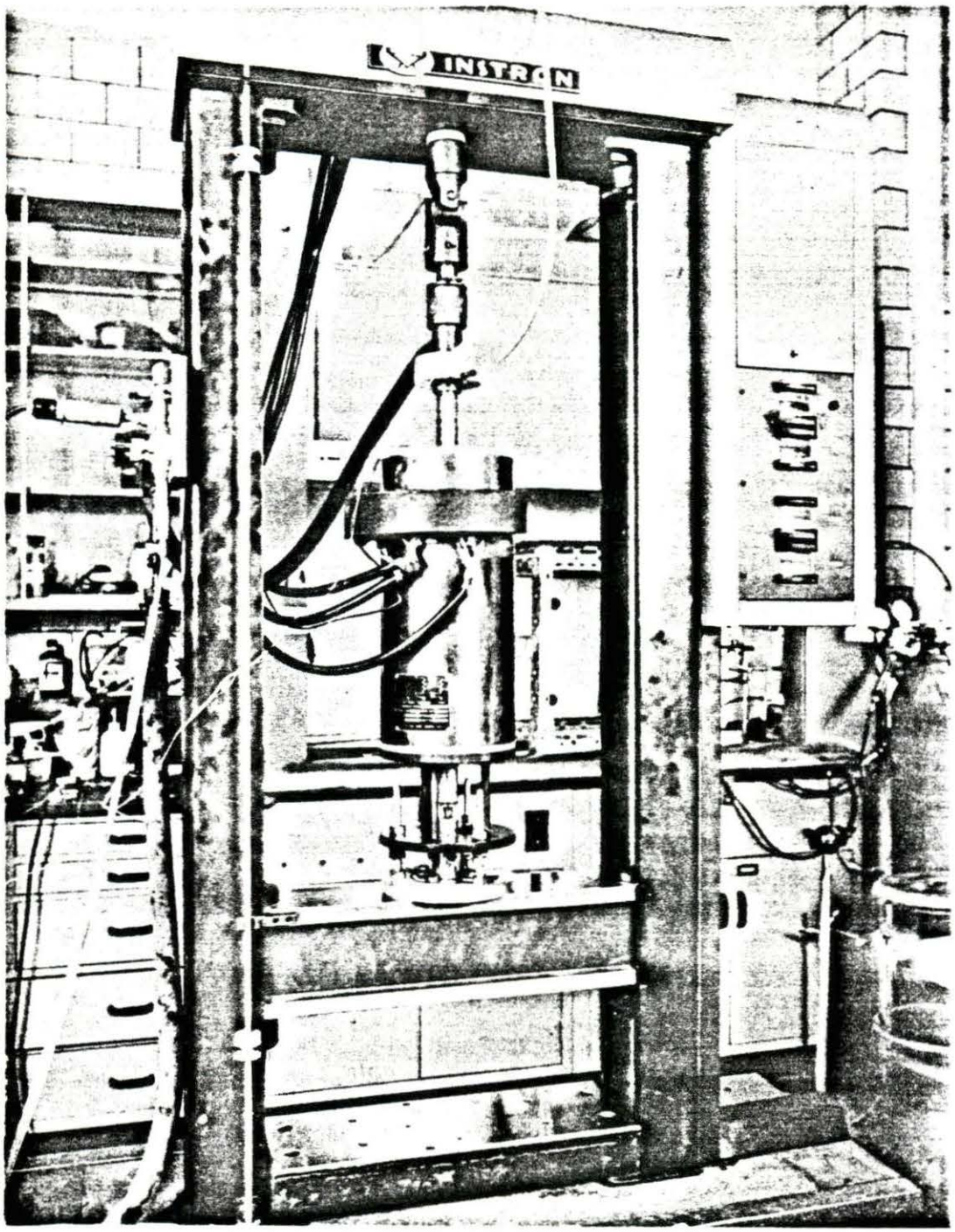

Figure 5. Load frame and the elevated temperature tensile test assembly

C. Tensile Tests

The crosshead speeds of 0.1 inch/minute and 0.01 inch/minute, and corresponding strip chart speeds of 5 inch/minute and 1 inch/minute were selected for this study. Before the tests, free running crosshead speed and strip chart speed were measured for the above-mentioned gear fitting using an electronic stop watch. The results of this verification showed good agreement with designed values.

For the elevated temperature tensile tests, furnace heating rates were measured using Bristol Model 570 12-channel recorder. Temperature versus time graphs for different controller voltage settings were obtained. Temperature indicating and recording instruments were verified using a potentiometer. Specimens from the grinder table showed small variation in width of the gauge section. Thickness of the specimen varied by small amounts from specimen to specimen. The thickness and width of each specimen's gauge section were measured at three different locations using a micrometer.

Room temperature tests were performed in air without the pull-rod vacuum jacket. Elevated temperature tensile tests were performed at temperatures ranging from 100°C to 800°C in 100°C steps. Each specimen was installed into the pin-type grips using a jig designed to prevent deformation of specimen during the fastening of four screws located in the corners of the grips. With specimen grips installed between the pull-rods, the vacuum jacket with assembled pull rods was inserted into the core of the cylindrical furnace by tilting the furnace. The threaded end of a lower pull-rod was attached to the mount on the moving crosshead, after which the upper pull-rod was attached to the flexible coupling by a pinned connection

using the "RETURN" control for crosshead movement. To prevent the twisting of the specimen during installation, special care was given to the setting of the pull-rod assembly in the vacuum jacket and to the pull-rod attachments at both the load cell and the crosshead.

To prevent the surface oxidation during heating and testing, the vacuum jacket was flushed several times with argon gas before and during heating. Elevated temperature tensile tests were performed at from 20 to 40 microns of vacuum. Forces acting on the load cell due to vacuum and friction were compensated by the balance control. Load calibration was performed for every four tests using ten 10-pound weights.

As described in the earlier section, load and displacement were recorded on the strip chart at the control console, and tensile properties of interest were determined from the chart. Percent elongation values were calculated from the initial gauge length and the time axis of the chart. The 0.2% offset yield stress and ultimate tensile stress were calculated from the measured gauge section dimensions and the load axis of the strip chart. Among three measured values of cross sectional area of the gauge section, the smallest value was used in this calculation. Reported strain rates of 2.2×10^{-3} and 2.2×10^{-4} per sec were calculated from the original gauge length and crosshead speeds.

Figure 6 shows typical heating curves used in these experiments. After obtaining the equilibrium temperature, tensile loading was applied within 3 and 7 minutes for strain rates of 2.2×10^{-3} and 2.2×10^{-4} per sec, respectively. Specimens fractured outside the gauge section were discarded and the test was repeated. For every temperature step, two to four specimens were used.

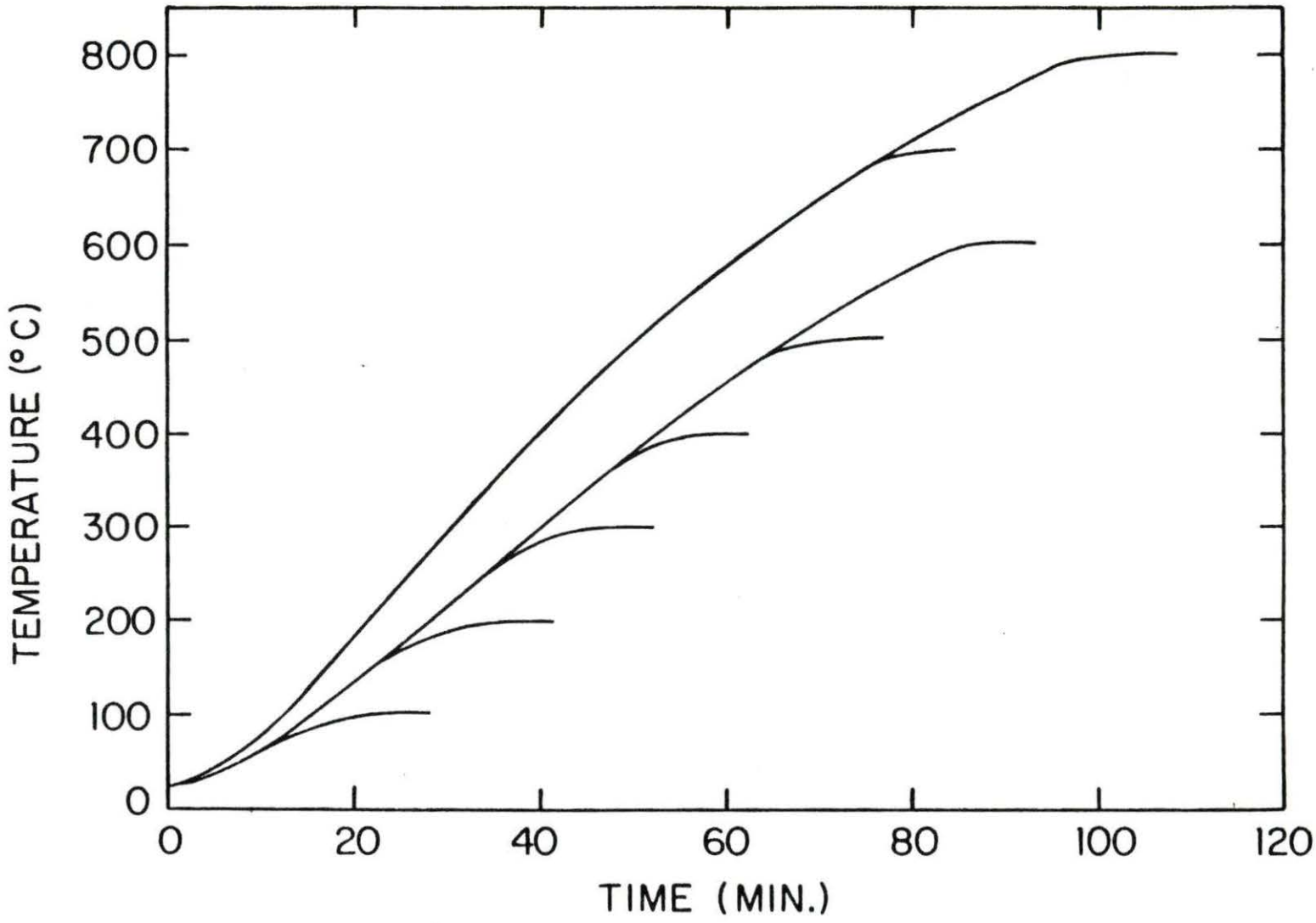

Figure 6. Typical specimen heating curves applied in the elevated temperature tensile tests.

D. Hardness Test Apparatus

Room temperature and elevated temperature microhardness tests were performed on the Elevated Temperature Microhardness Tester (ETMT), which was built at Ames Laboratory according to the design provided by the Oak Ridge National Laboratory (50). This ETMT is capable of performing hardness tests from room temperature up to 1000°C in vacuum or an inert gas atmosphere. Synthetic sapphire is used as an indenter in this ETMT because its high temperature properties are better than those of diamonds up to 1000°C (51, 52).

The ETMT used in this experiment consists of four main parts; indenter assembly and indenter positioning system, push-rod and specimen driving system, specimen heating furnace and temperature controller, and vacuum and cooling system. Figure 7 shows schematic view of testing chamber of ETMT.

The sapphire indenter is finished to have the same face angle of 136 degrees as for the Vickers diamond indenter and is mounted on the molybdenum holder which is screwed to an Inconel adapter. The Inconel adapter is connected to a threaded Al_2O_3 rod and then screw-connected to doughnut-shaped weights carrying a stainless steel rod. The weight carrying rod is guided axially by an unlubricated rolling bearing system with negligible friction. The indenter positioning system is operated by two sets of bevel gears and is capable of moving the indenter tip along two perpendicular directions (i.e., in a x and y grid system) using the dials located below the base plate.

The test specimen is located within the groove on the specimen holder and is fixed by a steel leaf spring. The specimen holder is put on the

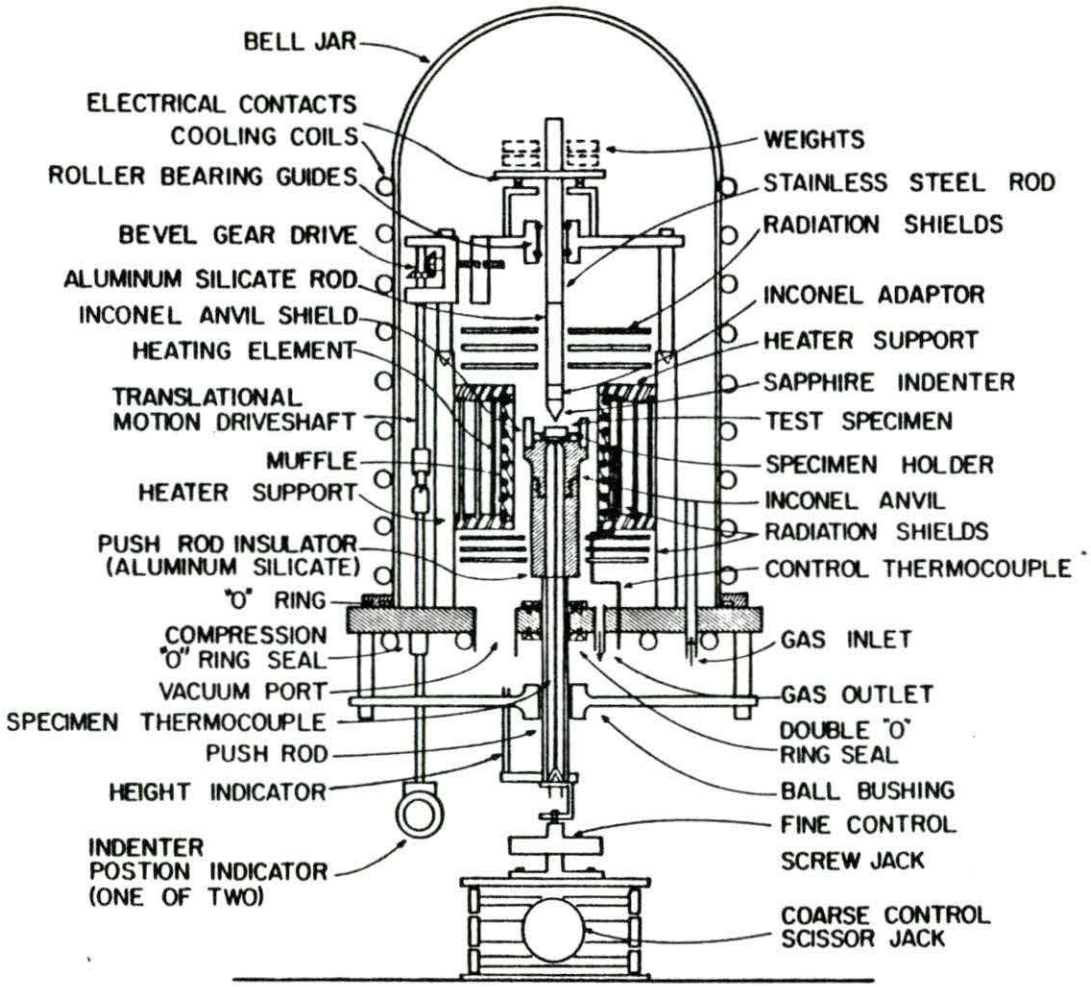

Figure 7. Schematic diagram of the elevated temperature microhardness tester

Inconel anvil which is screwed to the Al_2O_3 push rod shield and is secured by the set screws of the anvil shield to prevent movements of the specimen during the tests. The Inconel push-rod is guided by a ball bushing. The push rod and specimen driving system is furnished with coarse and fine control screw jacks to raise or lower the axial position of specimens. The coarse control scissor jack is usually used when there is a need to move the push rod by large amounts (i.e., at a time when installing or removing the indenter rod and specimen holder). During the tests, the specimen is lifted by the fine control screw jack. The application and removal of weights from the indenter tip and from the specimen surface are sensed by a control lamp, which is operated by three electrical contacts located on the top of the indenter housing.

The specimen heater is wound with a nickel-chromium coil element around a refractory cylinder. To minimize the heat losses to the surroundings, the heater is circumferentially surrounded by tantalum and stainless steel radiation shields. These are assembled into the furnace by the upper and lower heater supports. The upper heater support is made of an Al_2O_3 plate and the lower heating support is made of a dual Al_2O_3 and stainless steel plate. Upper and lower radiation shields are also installed outside the furnace.

The furnace temperature is monitored by means of a chromel-alumel thermocouple attached to the specimen heater wall. The specimen temperature is monitored by a similar thermocouple located at the upper tip of a thermocouple guide hole of the Inconel anvil. Furnace temperature is controlled by a keyboard command type 12-channel furnace controller. This

system operates by built-in programs in the memory units to provide the instruction stream for the central processing unit (CPU). Temperature monitoring of each channel is done by thermocouple input to the amplifier filter circuits. With simple input command through the keyboard, ramp increase of temperature with specified slopes, holding operations at a set temperature for a specified time, and successive display of different channel temperatures are possible. This system is also equipped with a variac, which permits manual adjustment of the heating rate of the furnace. During the tests, external monitoring of the specimen and furnace temperature is provided by an alternative digital display unit. Specimen temperatures are also recorded on a Bristol Model 560 temperature recorder.

A vacuum port on the base plate is connected to both mechanical and diffusion pumps. The testing chamber is also furnished with an inert gas inlet-outlet valve in order to provide a heating or testing in the inert gas atmosphere and for rapid cooling with inert gas flow. Combined operation of the mechanical and diffusion pumps can provide a vacuum of 10^{-5} torr. The cooling system provides separate cooling water circuits for the bell jar, the base plate, and the diffusion pump.

E. Hardness Tests

High temperature microhardness tests were performed at temperatures ranging from 50°C to 850°C in 50°C steps. Specimens were heated and tested in the vacuum of 7 microns (7×10^{-3} torr). To obtain good indentations, the indenter housing was aligned with respect to the anvil stage using a water level gauge. All through the tests, a load of 1.2 kg was applied.

The load application time was controlled to 15 ± 1 sec using a control lamp and an electronic stop watch.

Successive indentations were made according to the predetermined indentation scheme using the indenter tip positioning dials. From 15 to 20 impressions were made for every temperature step. Table 7 shows the specimen number and indentation scheme adopted in this experiment.

Table 7. Indentation schemes adopted in hot hardness tests

Sample No.	Test temperature (^{o}C)
#1	Room temperature, 50-300
#2	350-500
#3	550-700
#4	Room temperature 750-850

Both variac and 12-channel temperature controller were used in controlling the specimen temperature. The furnace heating rate was manually controlled by the variac. Typical specimen heating and testing curves are shown in Figure 8. In successive step tests, the time to reach equilibrium temperature ranged from 10 to 15 minutes. Usually, it took about 8 minutes to make 15 impressions. After the tests were completed, the specimen was cooled to room temperature under vacuum within the testing chamber. Room temperature hardness tests were performed in air without the bell jar.

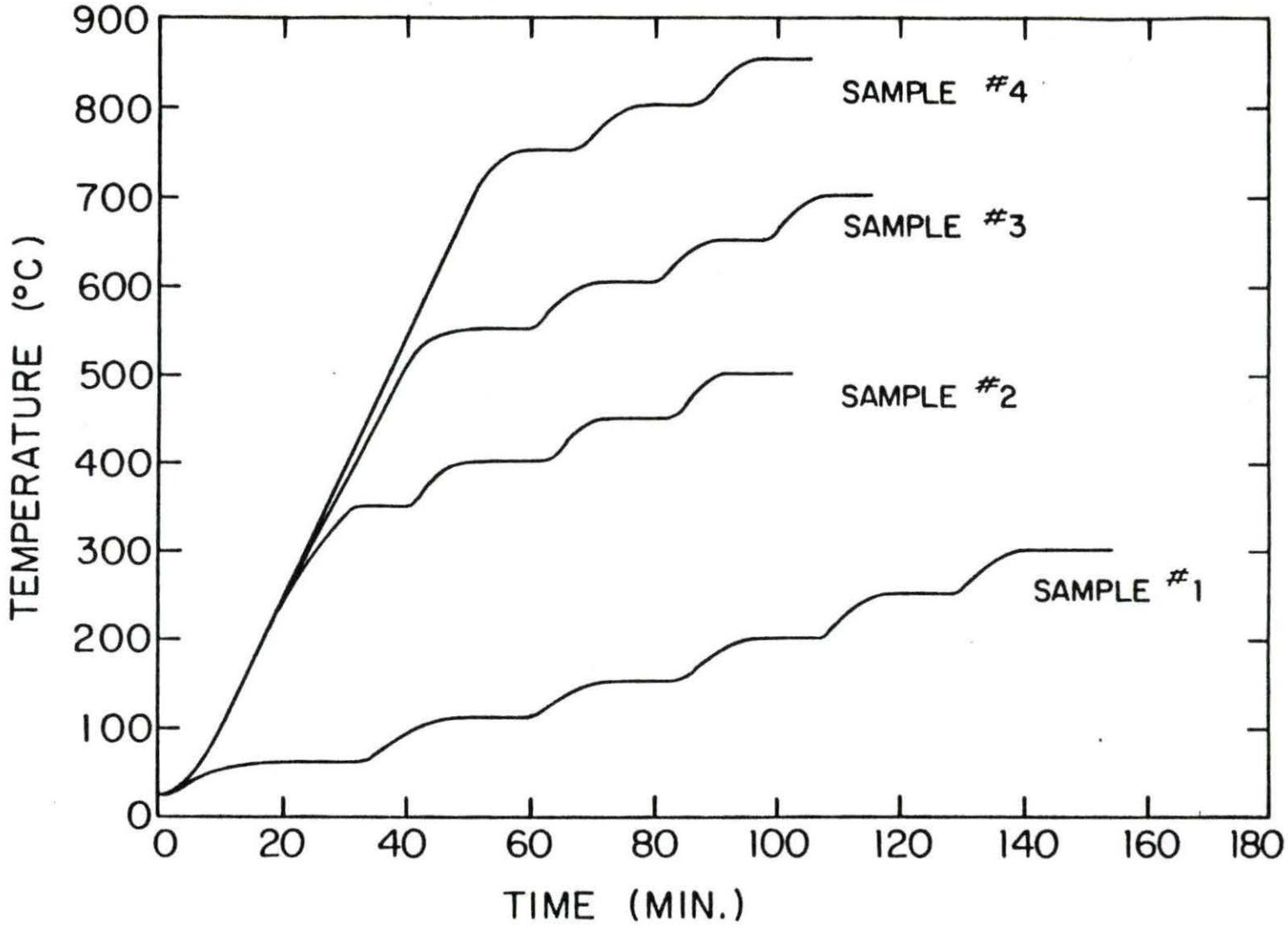

Figure 8. Specimen heating and testing curves applied in the high temperature microhardness tests.

The indenter tip was examined after every set of tests using 50x magnification of the indentations. Any specimen tested by a damaged indenter was discarded and a new specimen was retested with a new indenter. To keep the system free of vibration, the mechanical pump was turned off during the indentation tests.

The diagonal lengths of all impressions were measured in filar units at room temperature on the calibrated filar micrometer. This microscope is equipped with a field diaphram control and an aperture diaphram control. These controls were adjusted to give the best hardness impressions.

From the mean values of the measured diagonal length, the diamond pyramid hardness (DPH) number was calculated by dividing the applied load by the surface area of the impression (53-55). In this calculation, the following equation was used:

$$DPH = \frac{2P\sin(\theta/2)}{L^2} = \frac{1.854P}{L^2}$$

where

P = applied load, kg;

L = average length of diagonals, mm;

θ = angle between opposite faces of diamond = 136 degrees.

The correction for thermal contraction of indentations during cooling was neglected in this investigation.

III. RESULTS

A. General

Optical metallography performed on the slice from the as-received bar is shown in Figure 9. Dendritic structure shown in the optical micrographs of as-cast undoped and doped AL2 alloy is also presented in Figure 10. Results of the chemical analysis by inductively coupled plasma-atomic emission spectroscopy (ICP-AES) performed on the three different sections of the finger showed fairly good assimilation of yttrium by arc-melting and casting (Table 8).

Optical micrograph obtained from the homogenize-annealed piece (Figure 11) showed some difference in the size and distribution of second phases between undoped and doped alloy. There occurred fine inclusions within the grains for the doped alloy, while none of these were found in undoped specimens. Chemical compositions of the homogenize-annealed undoped and doped alloy obtained from atomic absorption spectroscopy analysis are tabulated in Table 9.

As is shown in Figure 12, optical micrographs of cold-rolled 30-mil sheet material showed stringers and fine inclusions disposed parallel to the rolling direction.[1] After final anneal of the tensile specimens, 1 hour at 1050°C, fine inclusions agglomerated and showed somewhat coarse distribution of the second phases (Figure 13).

Electron microprobe examination was performed to investigate the compositions of the second phases observed on the micrographs of the

---

[1] Amounts of stringers were found to be somewhat larger for doped specimen than for undoped specimen.

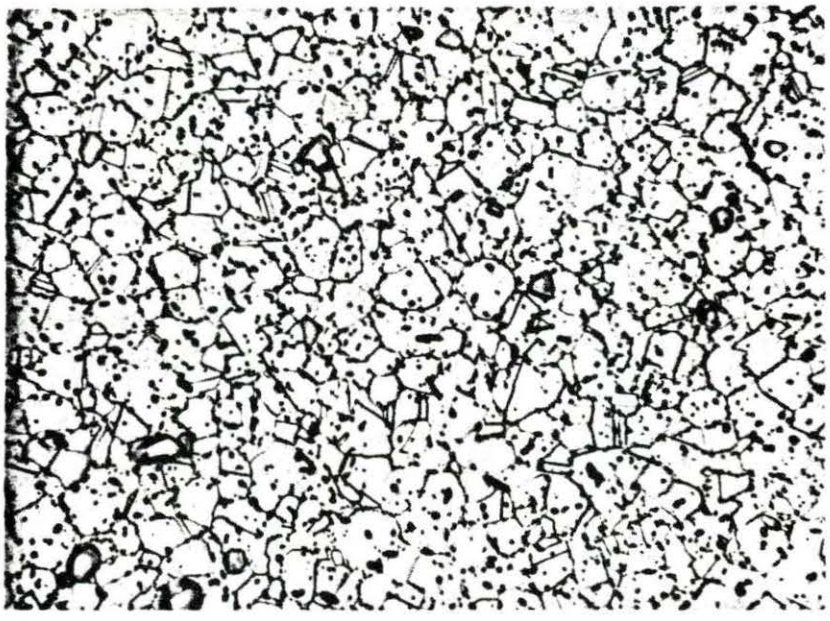

Figure 9. Optical micrograph of as-received AL2 alloy, electrolytically polished and etched with glyceregia (100X).

(a)

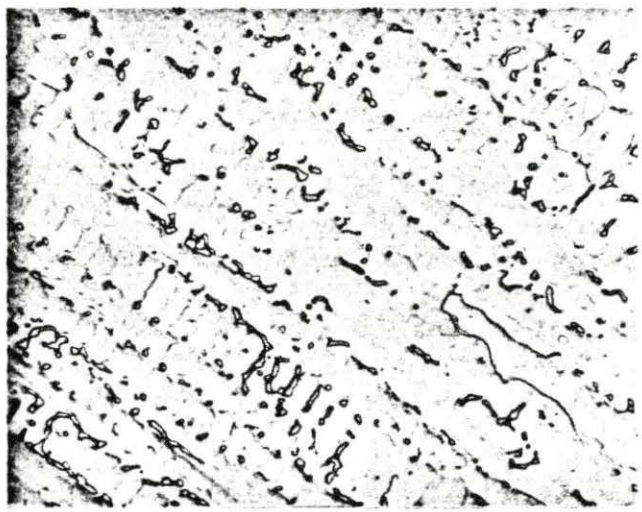

(b)

Figure 10. Optical micrographs of as-cast AL2 alloy (250X). Polished with Linde A and etched with glyceregia. (a) undoped, and (b) doped with 0.1% Y.

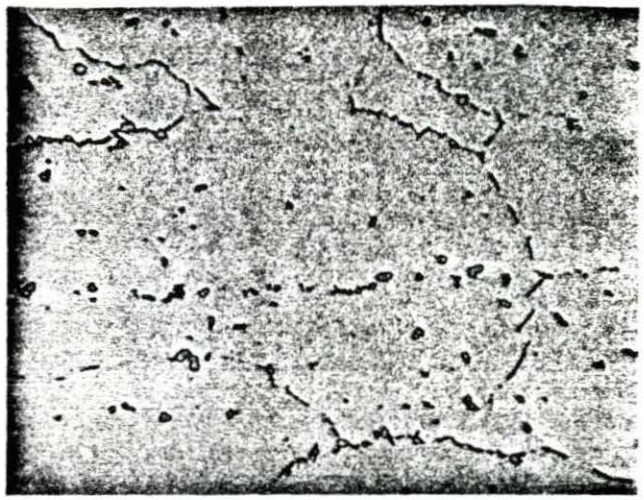

(a)

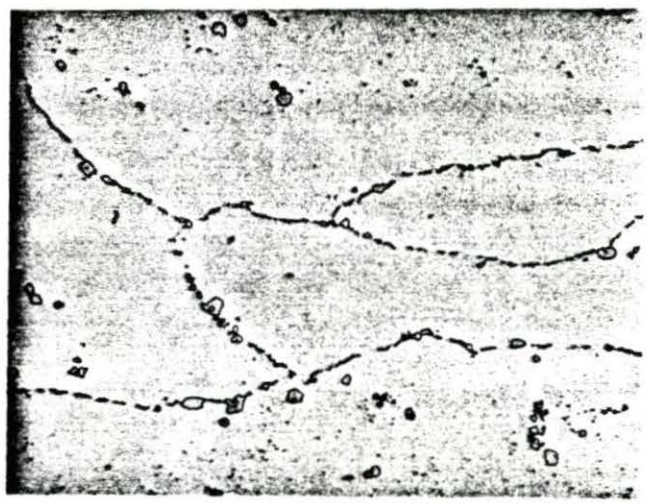

(b)

Figure 11. Optical micrographs of homogenize-annealed specimens (500X). Etched with glyceregia following Linde A polishing. (a) undoped, (b) doped with 0.1% Y.

Table 8. Results of chemical analysis on as-cast undoped and doped AL2 alloy

Element	Concentration (wt percent) Portion A	Portion B	Portion C	Average
Undoped				
Fe	49.2	47.6	50.2	49.0
Ni	33.0	32.5	31.6	32.4
Cr	12.1	12.0	11.9	12.0
Y	<0.001	<0.001	<0.001	<0.001
Doped				
Fe	49.8	50.1	49.5	49.0
Ni	33.4	32.5	31.6	33.0
Cr	12.1	12.0	11.9	12.0
Y	0.102	0.093	0.099	0.098

Table 9. Results of chemical analysis on as-homogenize-annealed undoped and doped AL2 alloy

Element	Concentration (wt percent) Portion A'	Portion B'	Portion C'	Average
Undoped				
Fe	47.75	48.01	48.56	48.11
Ni	33.80	33.53	33.50	33.61
Cr	12.32	12.36	12.43	12.36
Doped				
Fe	47.96	47.92	48.51	48.13
Ni	33.53	33.62	33.74	33.63
Cr	12.14	11.83	12.15	12.04
Y	0.11	0.13	0.11	0.117

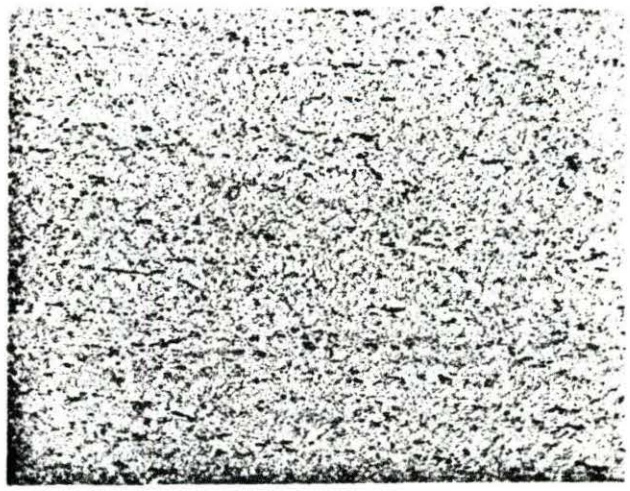

(a)

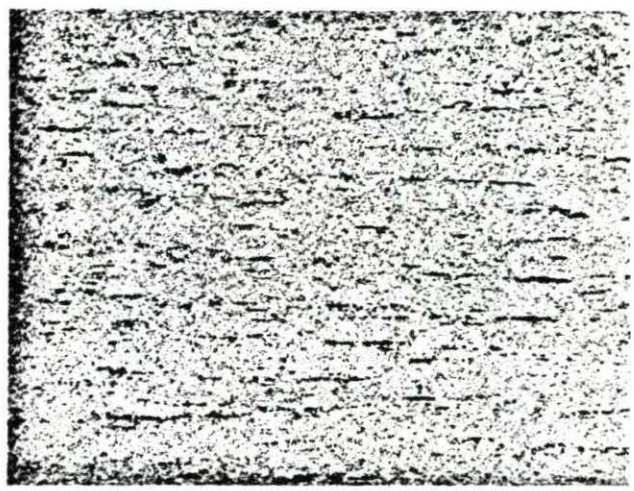

(b)

Figure 12. Optical micrographs of undoped and doped AL2 alloy (100X). 30-mil thick sheets in cold-rolled condition, cold mounted and etched electrolytically with oxalic acid following Linde A polishing. (a) undoped, and (b) doped with 0.1% Y.

(a)

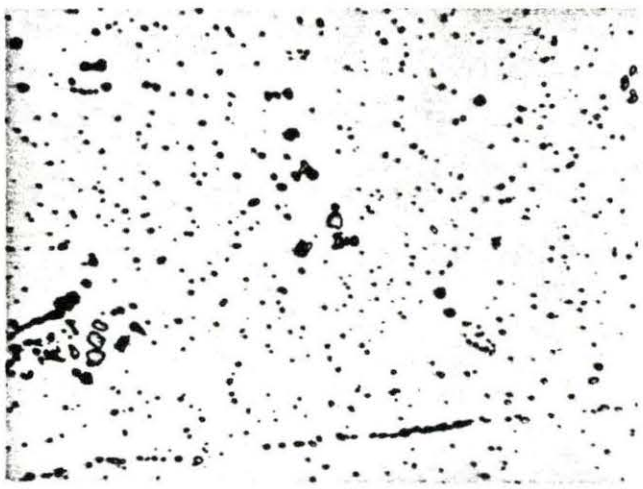

(b)

Figure 13. Optical micrograph of tensile specimen (500X). Cold-rolled, annealed, ground and finally annealed at 1050 C for 1 hr. Electrolytically etched with oxalic acid following Linde A polishing. (a) undoped, and (b) doped with 0.1% Y.

homogenize-annealed (Figure 11) and cold-rolled material (Figure 14). Figures 15 and 16 show specimen current images of the undoped and doped alloy in the homogenize-annealed and cold-rolled (60-mil sheet) conditions. For both conditions, large black spots shown in Figure 15 and 16 tended to contain higher concentrations of Nb and Ti than the matrix. Bright spots were found to have lower concentrations of Nb and Ti than black spots, but to have higher concentrations of these elements than matrix. The Ti/Ni ratio at the investigated second phases was not found to be constant, but evidently suggested that these phases are composed of various amounts of Ni, Nb and Ti. It was also found that Nb and Ti are somewhat concentrated at the grain boundary inclusions. For the doped specimens, both for the homogenize-annealed and cold-rolled conditions, yttrium concentrations in the matrix were found to be far lower than the doping level, while showing about twice the doping level at grain boundaries and at the Nb- and Ti-rich inclusions. The fine precipitates observed within the grains of as-homogenize-annealed doped alloy (Figure 11-b) could not be analyzed with this technique.

Room temperature hardness for the as-received bar, as-cast and as-homogenize-annealed alloy are presented in Table 10. The highest room temperature hardness of the homogenize-annealed specimen suggests some hardening during the slow cooling within the furnace.

Analytical results of the atomic absorption spectroscopy analysis performed on the 30-mil and 60-mil sheets material for six undoped and doped alloys are listed in Table 11. The results on the doped alloys showed somewhat lower contents of yttrium than the doping level for Fingers #2 and #3. To obtain consistent data for the high temperature tensile and

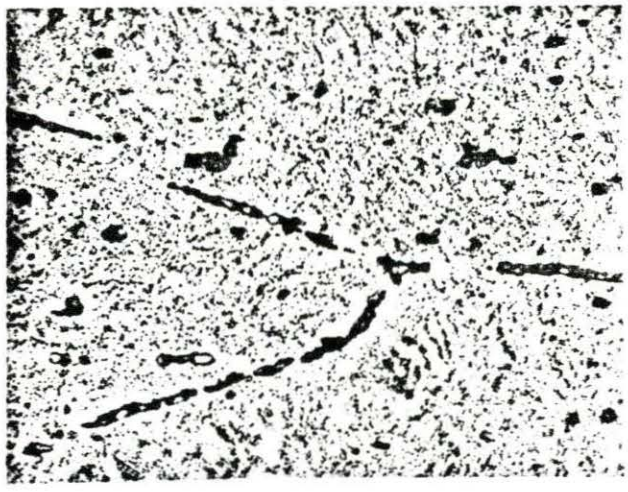

(a)

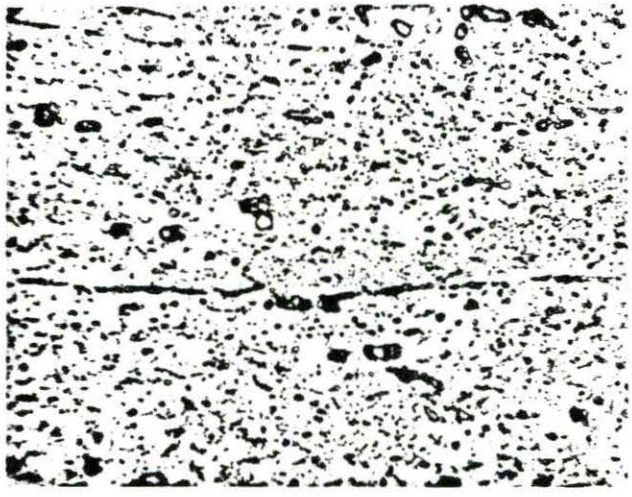

(b)

Figure 14. Optical micrographs of AL2 alloy (500X). 60-mil thick hardness specimens in cold-rolled condition, cold mounted, Linde A polishing and electrolytically etched with oxalic acid. (a) undoped, and (b) doped with 0.1% Y.

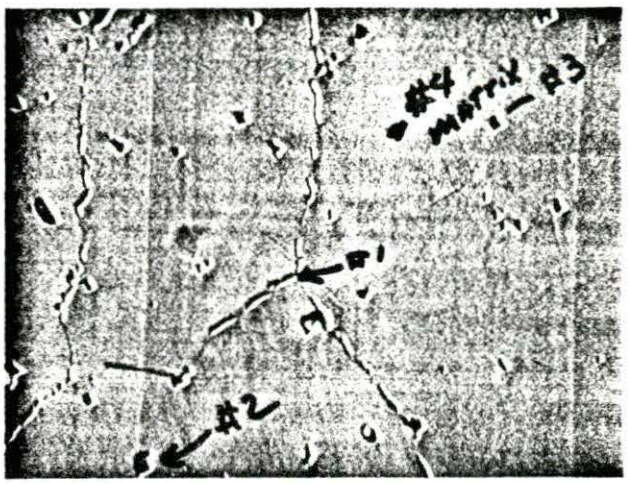

(a)

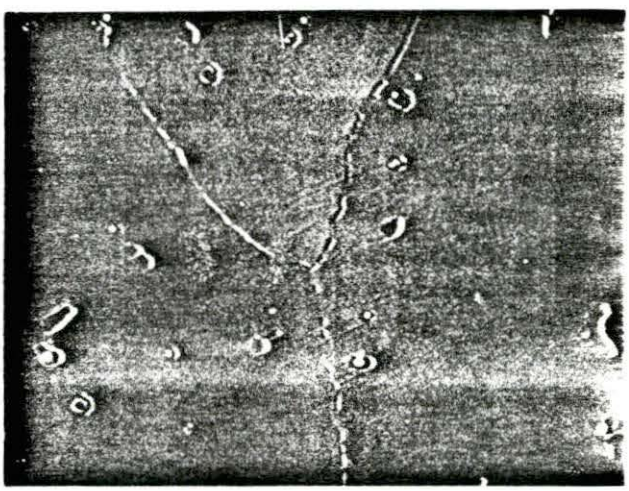

(b)

Figure 15. Specimen current images of as-homogenize-annealed specimens (1000X). (a) undoped, and (b) doped with 0.1% Y.

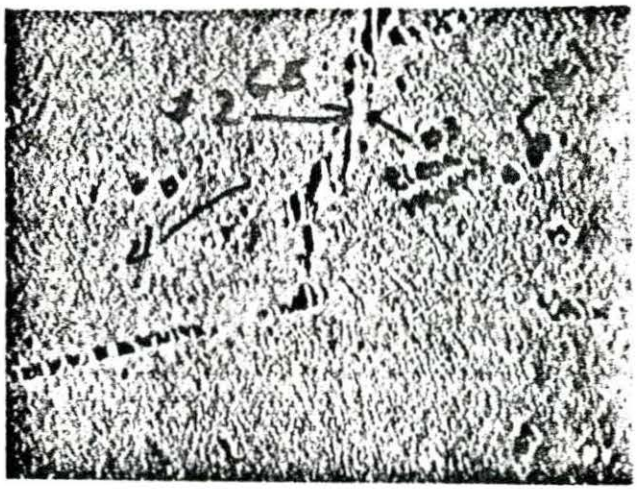

(a)

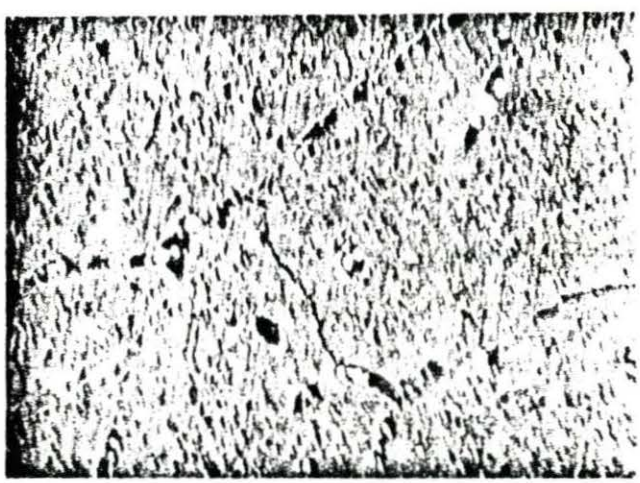

(b)

Figure 16. Specimen current images of AL2 alloy specimens taken from 60-mil sheets in cold-rolled state (1000X). (a) undoped, and (b) doped with 0.1% Y.

hardness tests, specimens from Finger #1 were used in tensile tests and specimens from Finger #2 and Finger #3 were used in hardness tests.

Table 10. Room temperature hardness of undoped and doped AL2 alloy

Description of sample	Hardness (DPH)	
	Undoped	Doped
As-received bar	167.2 ± 2.7	---
As-cast	142.b ± 4.1	141.7 ± 2.9
As-homogenize-annealed	269.6 ± 6.5	276.1 ± 7.5

Table 11. Results of chemical analysis on 30-mil sheets for undoped and doped alloy

Element	Concentration (wt percent)		
	Finger #1	Finger #2	Finger #3
Undoped			
Ni	34.1	34.1	34.0
Cr	12.4	12.4	12.4
Y	--	--	--
Doped			
Ni	34.0	34.0	34.0
Cr	12.4	12.4	12.4
Y	0.10	0.08	0.08

B. Tensile Tests

The results of tensile tests for strain rates of $2.2 \times 10^{-3}sec^{-1}$ and $2.2 \times 10^{-4}sec^{-1}$ and test temperatures from room temperature to 800°C performed on the undoped AL2 alloy specimens are shown in Figures 17-20. The corresponding tabulated information is given in Table 12. The error bars in Figures 17-20 indicate the higher and lower values obtained. For the yield stress at lower temperatures, the undoped alloy AL2 shows essentially no strain rate dependence (Figure 17), although there is some indication of higher yield stresses for the lower strain rate at 500-700°C. For both strain rates, there appears to be a yield stress peak at 700°C. The ultimate tensile stress shows a smooth decrease over the entire temperature range and very little strain rate dependence (Figure 18). The yield and ultimate tensile stresses are quite constant from 200 to 600°C. As seen in Figures 19 and 20, the ductility parameters, uniform and fracture strains, appear to be little affected by strain rate, except possibly at 100-600°C where the uniform and fracture strains are higher for the lower strain rate. An important feature shown in Figure 19 is the decrease in uniform strain that occurs for both strain rates above 500°C. This is a consequence of the decrease in the rate of work hardening above this temperature. This is shown in the stress-strain curves of Figure 21 for the undoped AL2 alloy at temperatures of 25, 305, 700, and 800°C and strain rate $2.2 \times 10^{-3}sec^{-1}$. Figure 21 also shows that serrated or dynamic yielding takes place at 305°C. This is further discussed below.

For the doped specimens, the results of tensile tests as a function of temperature and strain rate are shown in Figures 22-25. Table 13 shows

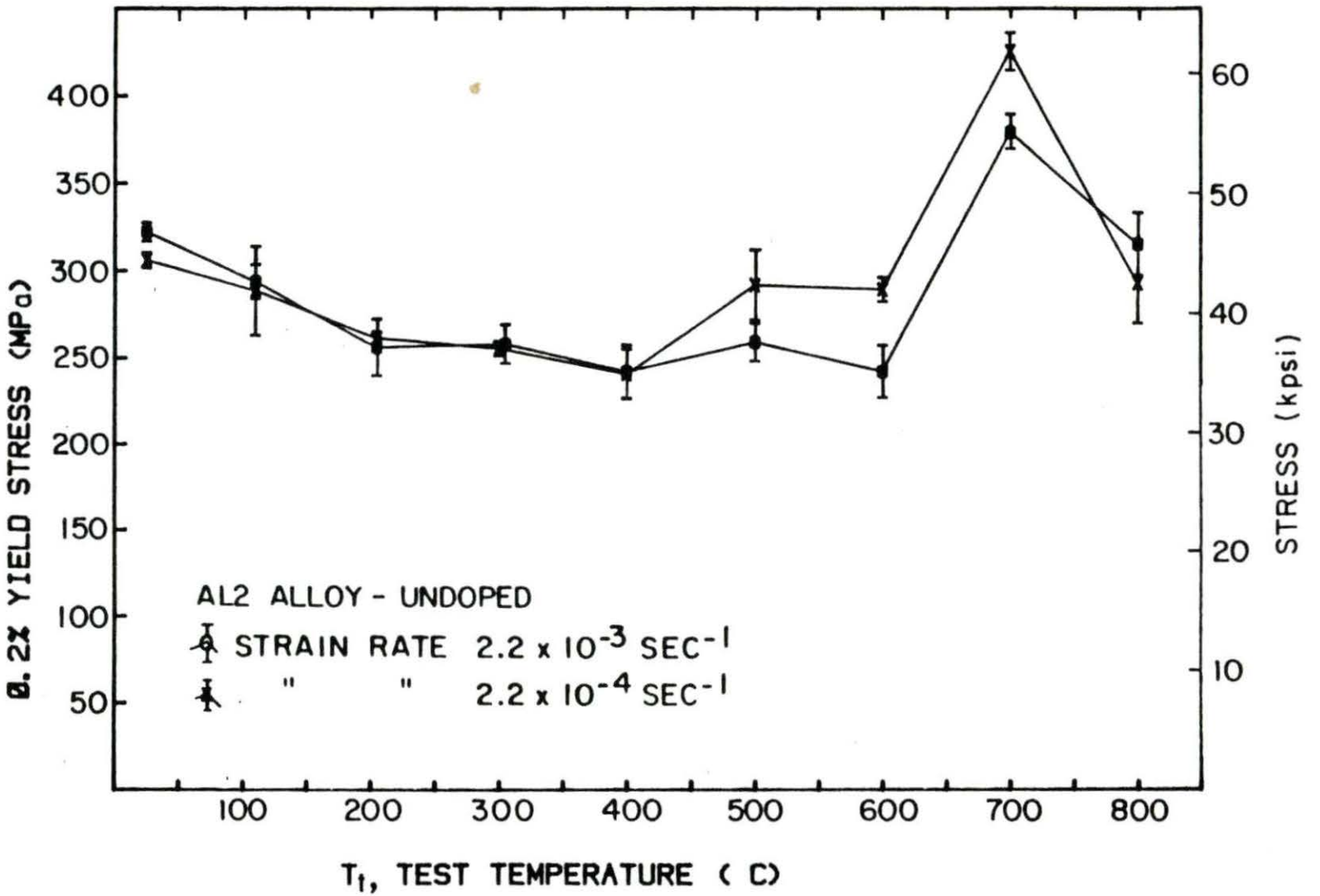

Figure 17. 0.2 percent yield stress of undoped AL2 alloy as a function of temperature for two different strain rates.

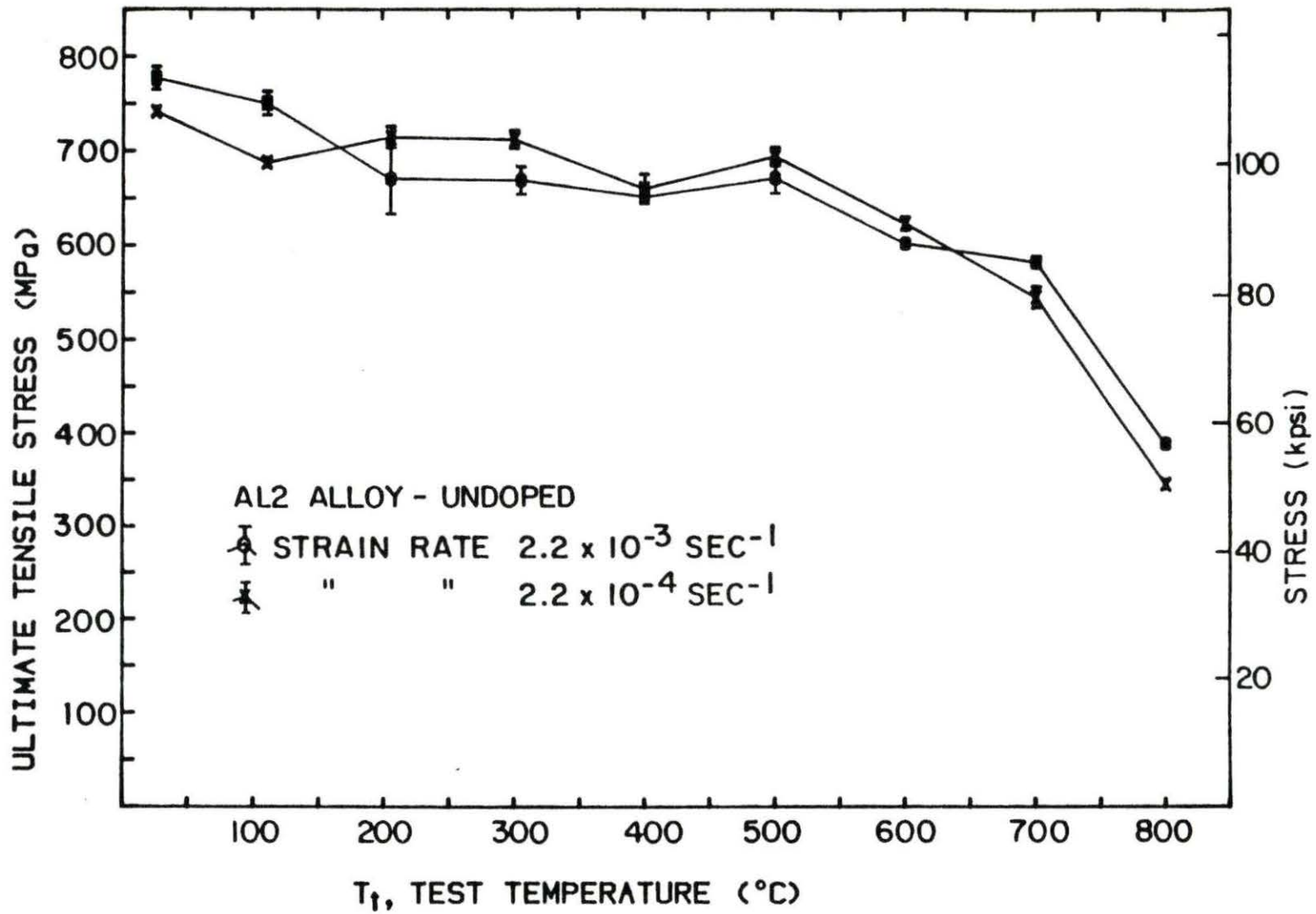

Figure 18. Ultimate tensile stress of undoped AL2 alloy as a function of temperature for two different strain rates.

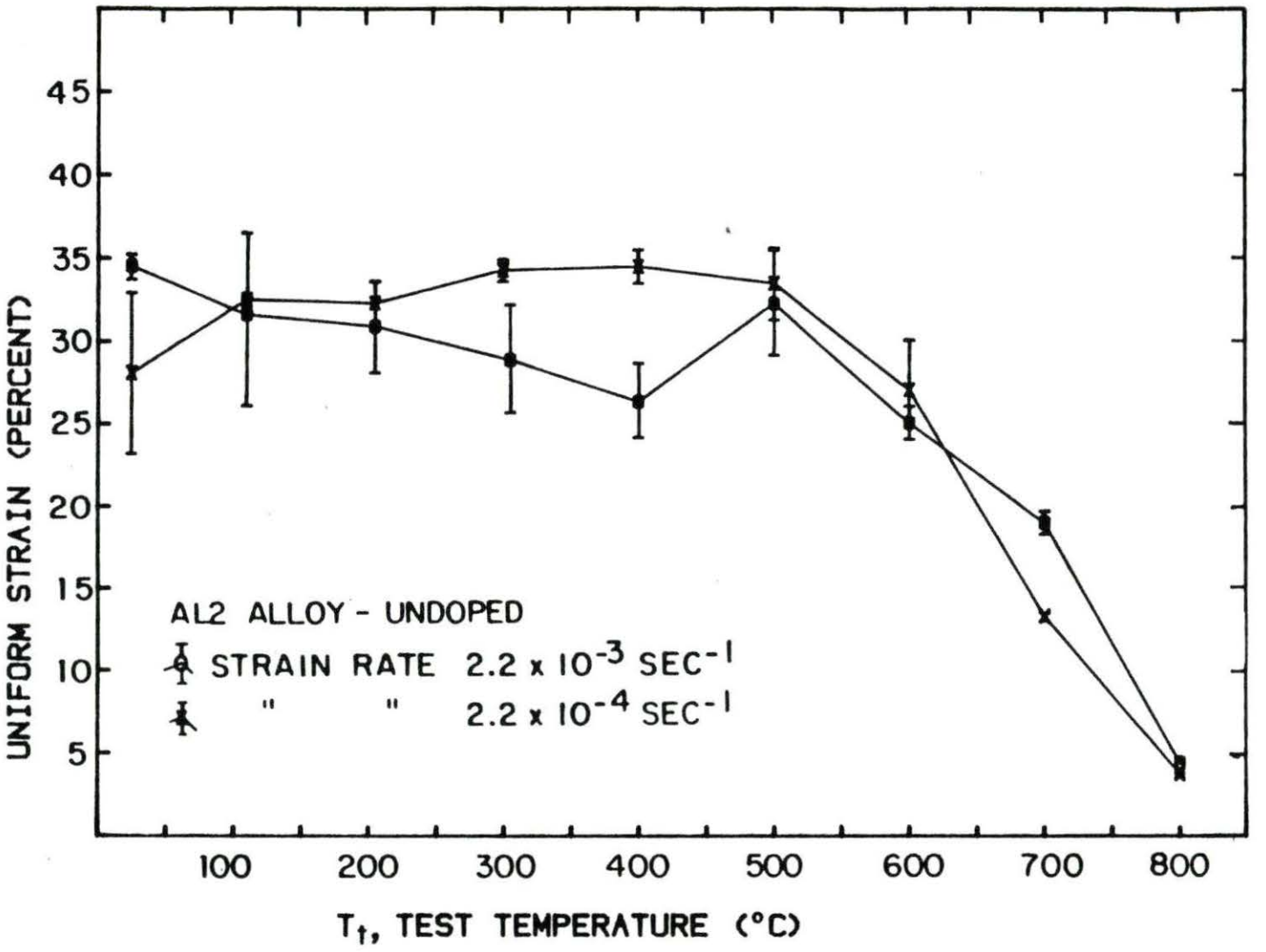

Figure 19. Uniform strain of undoped AL2 alloy as a function of temperature for two different strain rates.

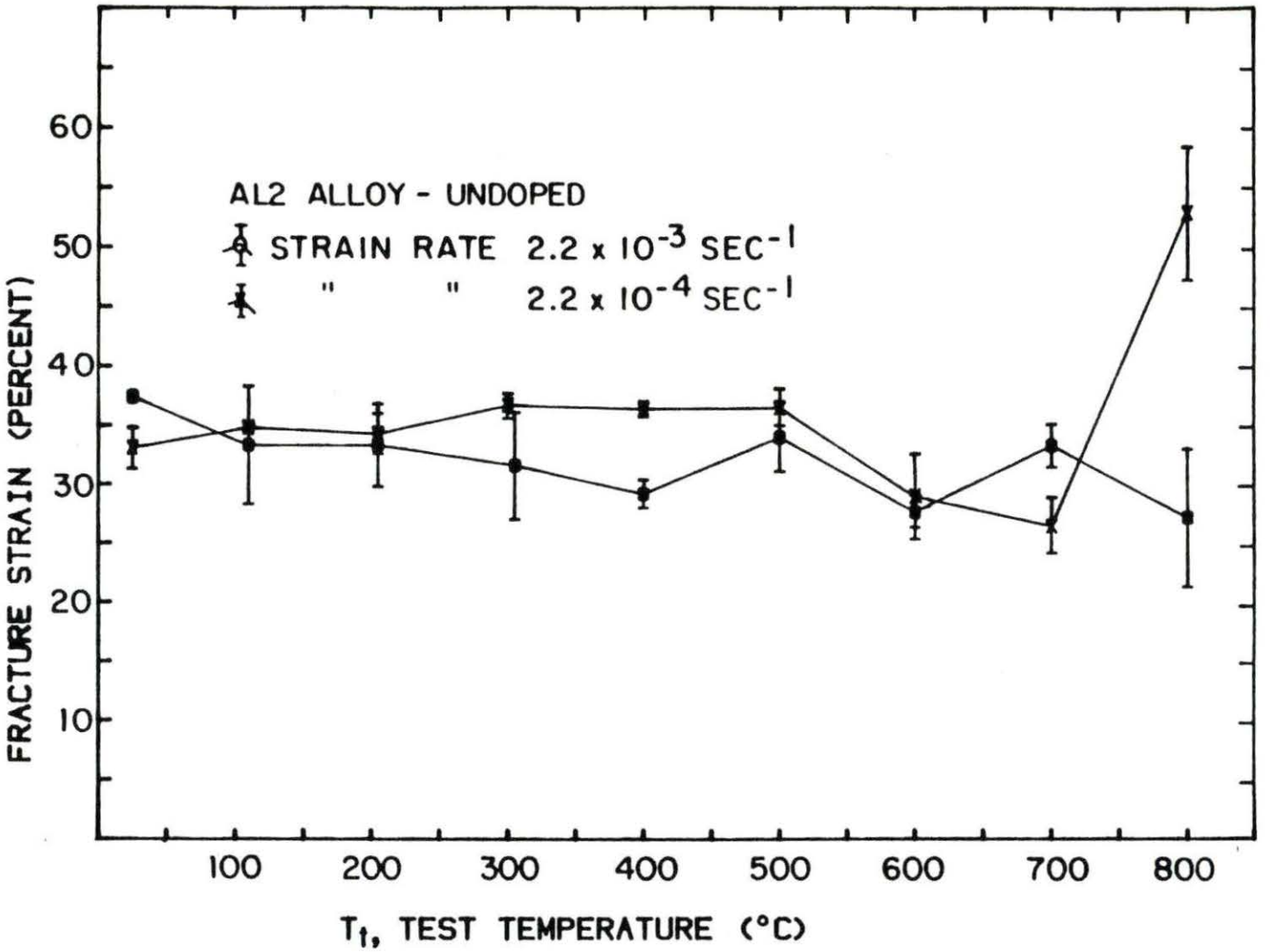

Figure 20. Fracture strain of undoped AL2 alloy as a function of temperature for two different strain rates.

Table 12. Tensile properties of undoped Fe-34% Ni-12% Cr AL2 alloy

Temperature (°C)	Stress, MPa (kpsi)		Elongation (percent)	
	Yield	Ultimate	Uniform	Fracture
	Strain rate - 2.2 x10^{-3}sec^{-1}			
25	322.2 (46.7)	776.5 (112.6)	34.5	37.4
110	293.9 (42.6)	750.2 (108.8)	31.6	33.3
205	256.1 (37.1)	670.4 (97.2)	30.9	33.3
305	258.3 (37.5)	668.8 (97.0)	28.9	31.6
400	242.3 (35.1)	651.5 (94.5)	26.4	29.2
500	259.2 (37.6)	671.2 (97.3)	32.3	34.0
600	242.4 (35.2)	602.3 (87.3)	25.1	27.7
700	379.2 (55.0)	582.4 (84.5)	19.0	33.3
800	315.2 (45.7)	389.2 (56.4)	4.4	27.2
	Strain rate - 2.2 x 10^{-4}sec^{-1}			
25	306.1 (44.4)	741.1 (107.5)	28.1	33.1
110	288.7 (41.9)	687.7 (99.7)	32.5	34.8
205	261.5 (37.9)	714.5 (103.6)	32.3	34.3
300	255.6 (37.1)	712.0 (103.2)	34.3	36.7
400	240.9 (34.9)	660.1 (95.7)	34.5	36.4
500	292.0 (42.3)	694.1 (100.7)	33.5	36.5
600	289.4 (42.0)	623.3 (90.4)	27.1	29.0
700	425.4 (61.7)	545.2 (79.1)	13.3	26.5
800	289.4 (42.0)	345.5 (50.1)	3.7	52.8

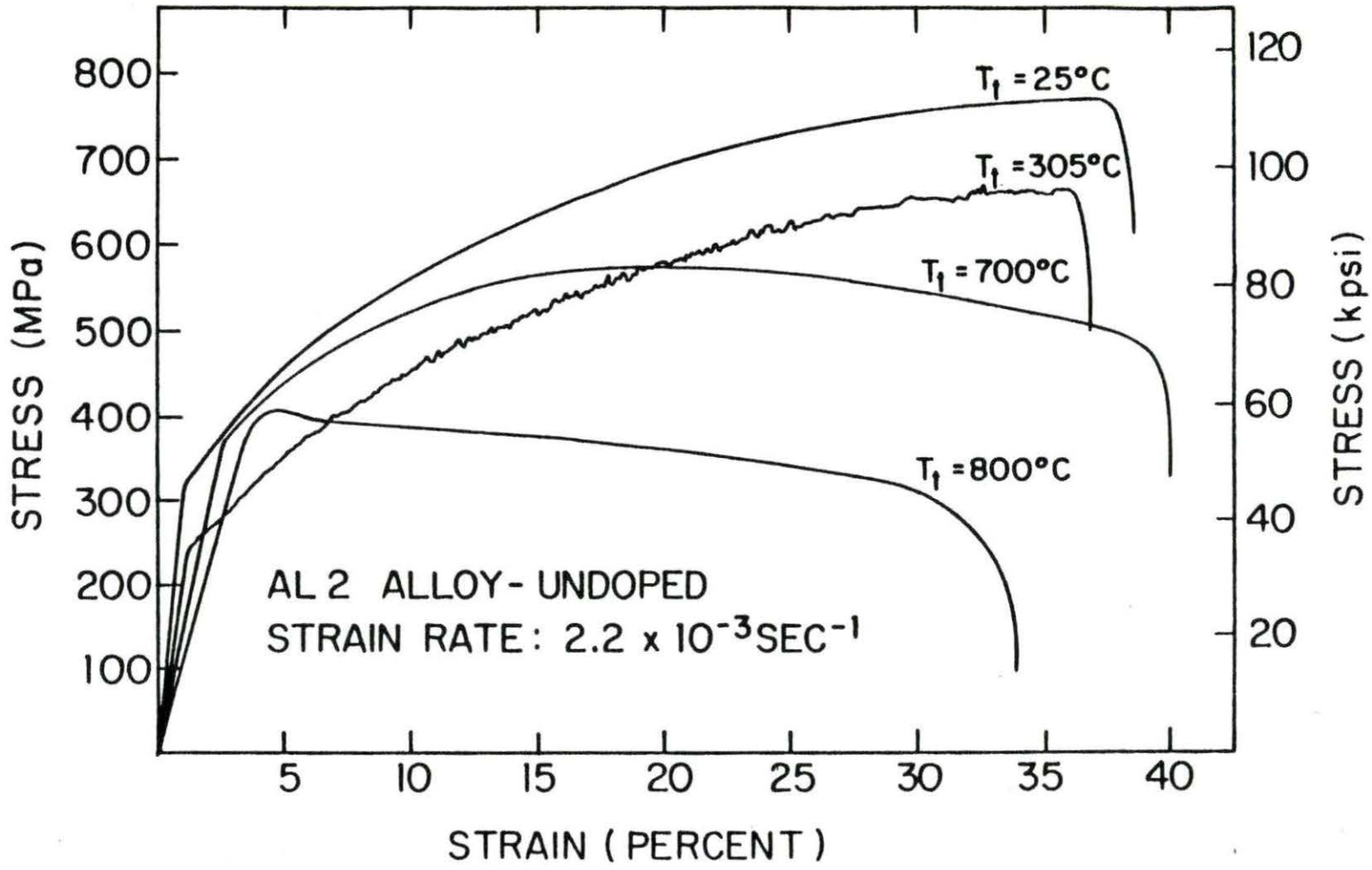

Figure 21. Stress versus strain for undoped AL2 alloy tested at 25, 305, 700, and 800 C at strain rate of 2.2 x 10^{-3}sec^{-1}.

the same information in tabular form. In contrast to the undoped specimen, the doped ones exhibit some strain rate dependence of yield stress in the temperature range from room temperature to 400°C (Figure 22). Above 400°C, the yield stress shows little strain rate dependence. The ultimate tensile stress is quite constant and strain rate independent from 100 to 600°C (Figure 23). Figures 24 and 25 show little strain rate dependence for the uniform or fracture strain, respectively. Again, there is a sharp drop in uniform strain above 600°C (Figure 24). Figure 26 shows the stress-strain curves for doped samples tested at 25, 300, 700, and 800°C and at $2.2 \times 10^{-3} sec^{-1}$ strain rate. The decrease in uniform strain above 600°C is apparent. For both strain rates, the fracture strain at 800°C varied greatly from specimen to specimen, but the general trend indicated large increases in fracture strain at this temperature, as is seen in Figure 25. Visual inspection of tested specimens showed necking at the fracture for samples tested at 800°C.

A major purpose of this investigation is to determine the effect of yttrium additions on the mechanical properties of the AL2 alloy. The tensile properties of the undoped alloy and the alloy doped with 0.1% Y are compared in Figures 26-30 for the higher strain rate and in Figures 31-34 for the lower strain rate. It is evident in Figures 27 and 31 that the yttrium doping produces a decrease in the yield stress for both strain rates over the entire temperature range from room temperature to 800°C, although the decrease in yield stress is somewhat greater for the lower strain rate. This is also largely the case for the ultimate tensile stress (Figures 28 and 32). On the whole, there appears to be little effect of the yttrium doping on the uniform strain (Figures 29 and 33)

Table 13. Tensile properties of doped Fe-34% Ni-12% Cr AL2 alloy

Temperature (°C)	Stress, Mpa (kpsi)		Elongation (percent)	
	Yield	Ultimate	Uniform	Fracture
	Strain rate - 2.2×10^{-3} sec^{-1}			
25	289.4 (42.0)	721.2 (104.6)	33.8	35.6
110	264.8 (38.4)	670.6 (97.2)	28.2	29.2
200	240.0 (34.8)	673.1 (97.6)	27.8	29.0
300	232.8 (33.8)	649.7 (94.2)	31.6	33.5
400	200.9 (29.1)	597.0 (86.6)	32.3	34.6
500	222.8 (32.3)	587.4 (85.2)	31.0	33.2
600	235.8 (34.2)	596.3 (86.5)	30.5	32.3
700	346.3 (50.2)	575.7 (83.5)	20.3	28.5
800	276.8 (40.1)	295.0 (42.8)	4.9	43.0
	Strain rate - 2.2×10^{-4} sec^{-1}			
25	241.7 (35.1)	695.3 (100.8)	30.5	32.2
110	220.7 (32.0)	642.0 (93.1)	27.0	28.2
200	207.0 (30.0)	678.4 (98.4)	31.3	32.2
300	211.4 (30.7)	659.0 (95.6)	31.3	33.9
400	212.2 (30.8)	634.7 (92.0)	35.7	37.6
500	219.6 (31.8)	617.9 (89.6)	27.2	29.0
600	248.5 (36.0)	619.3 (89.8)	32.4	34.4
700	306.3 (44.4)	515.6 (74.7)	16.2	30.1
800	307.0 (44.5)	334.1 (48.5)	3.9	49.7

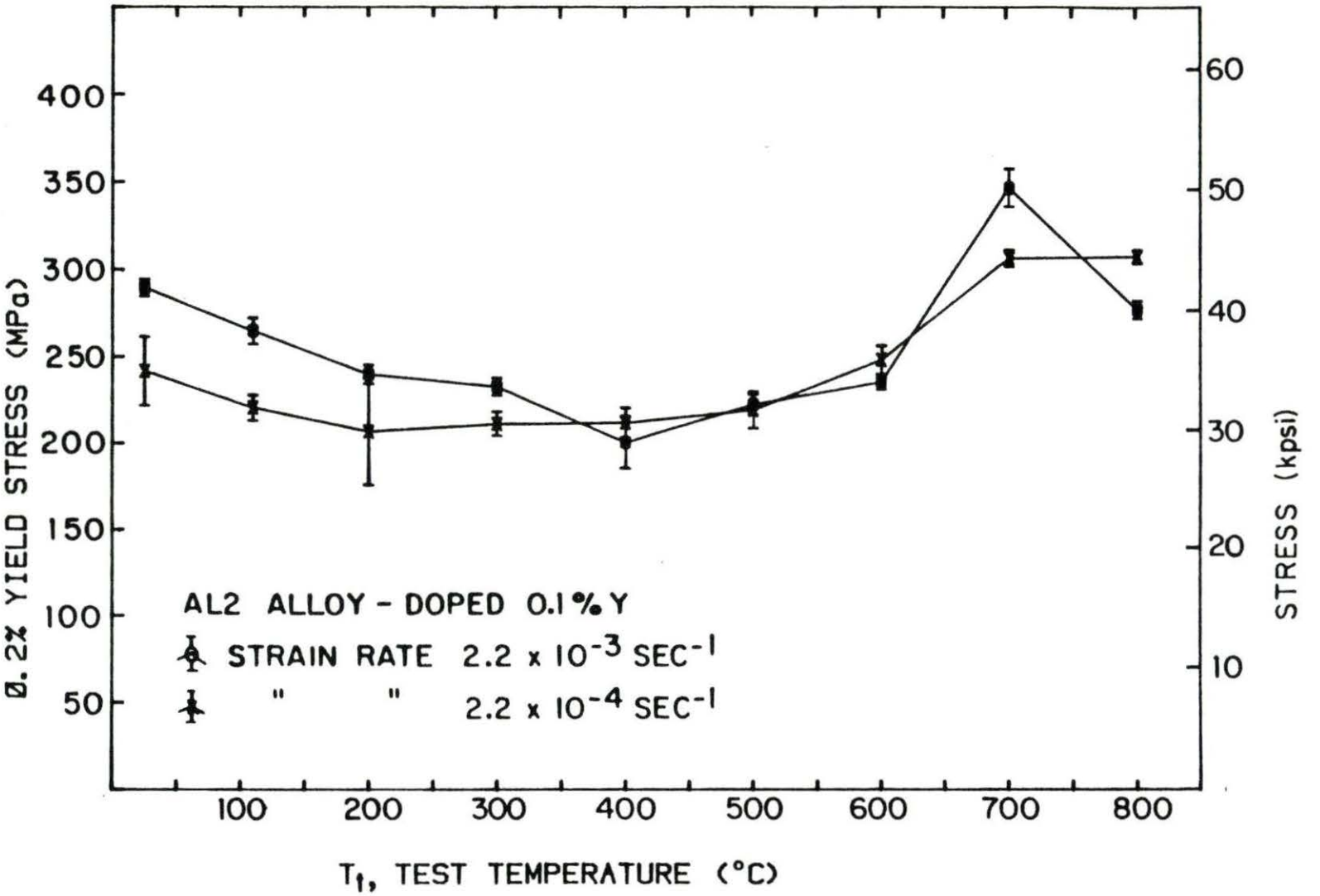

Figure 22. 0.2 percent yield stress of doped Al2 alloy as a function of temperature for two different strain rates.

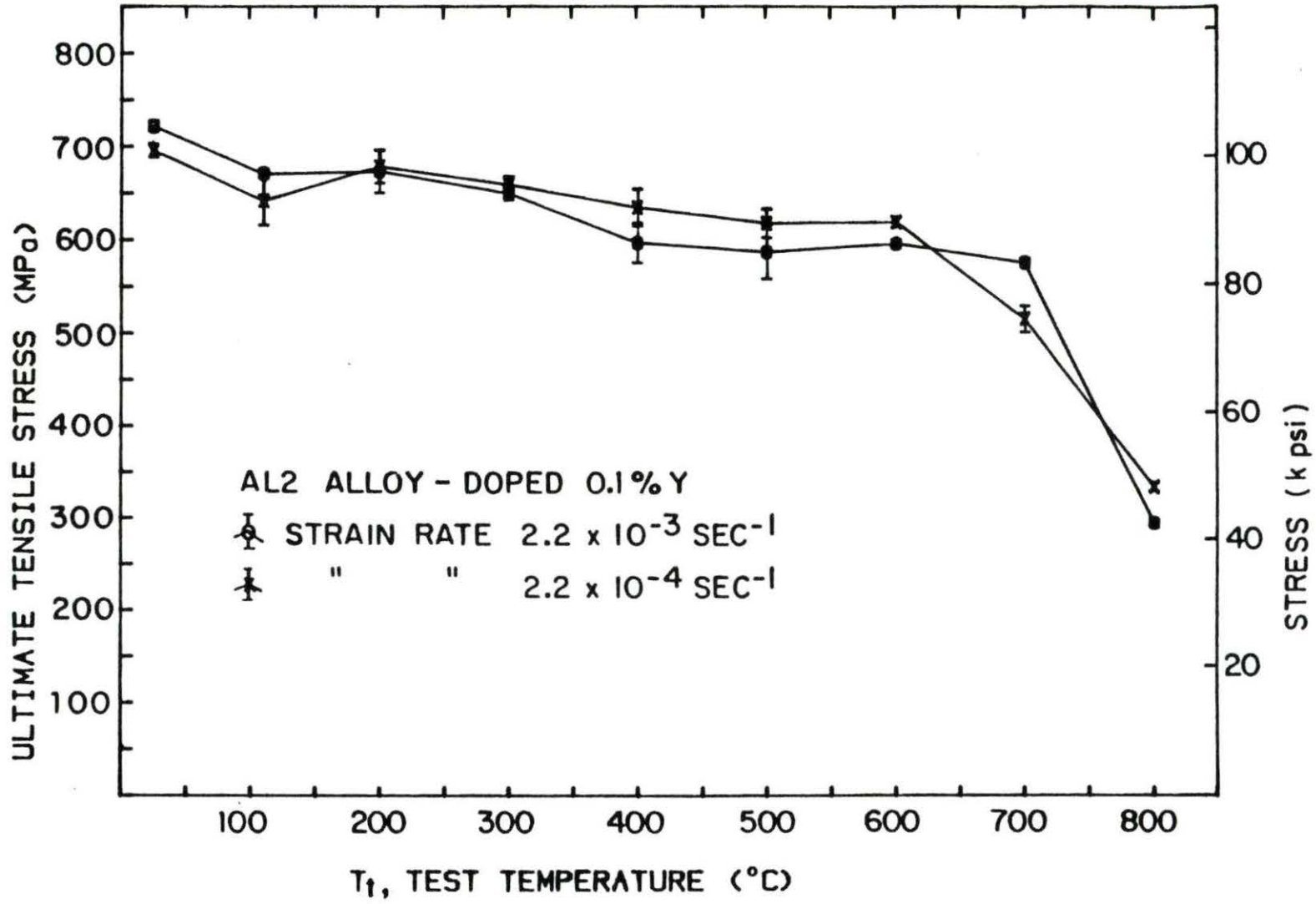

Figure 23. Ultimate tensile stress of doped AL2 alloy as a function of temperature for two different strain rates.

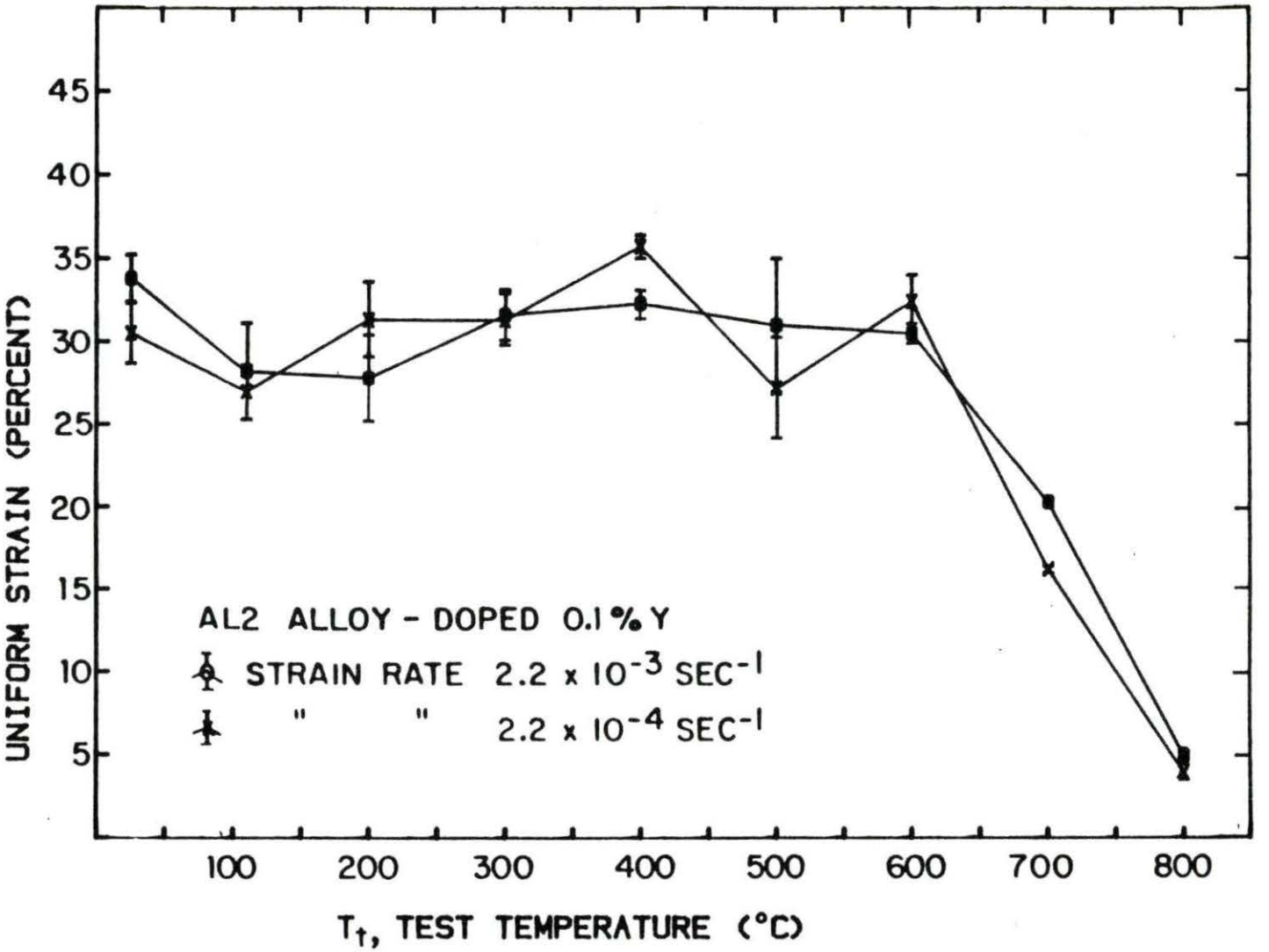

Figure 24. Uniform strain of doped AL2 alloy as a function of temperature for two different strain rates.

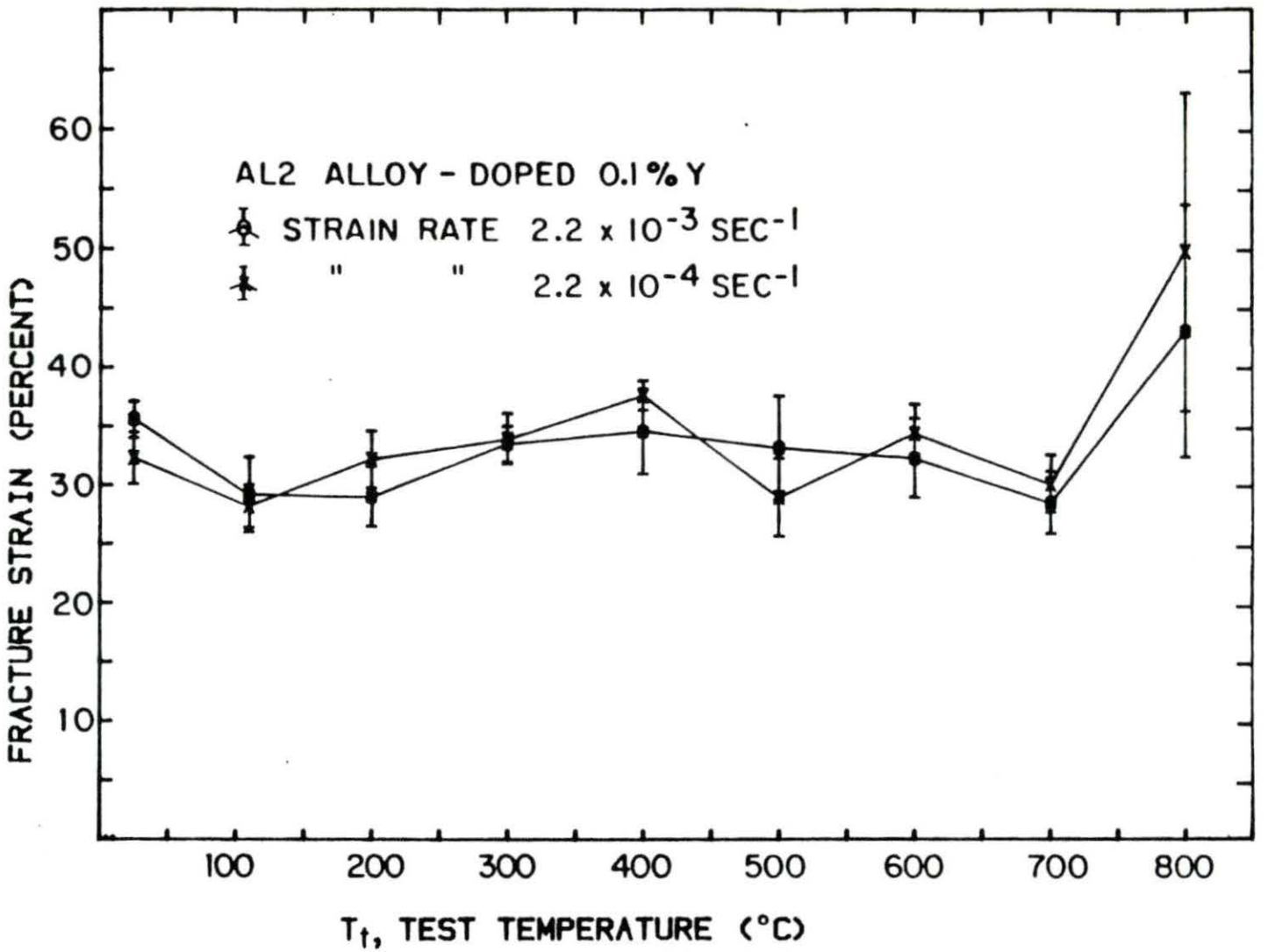

Figure 25. Fracture strain of doped AL2 alloy as a function of temperature for two different strain rates.

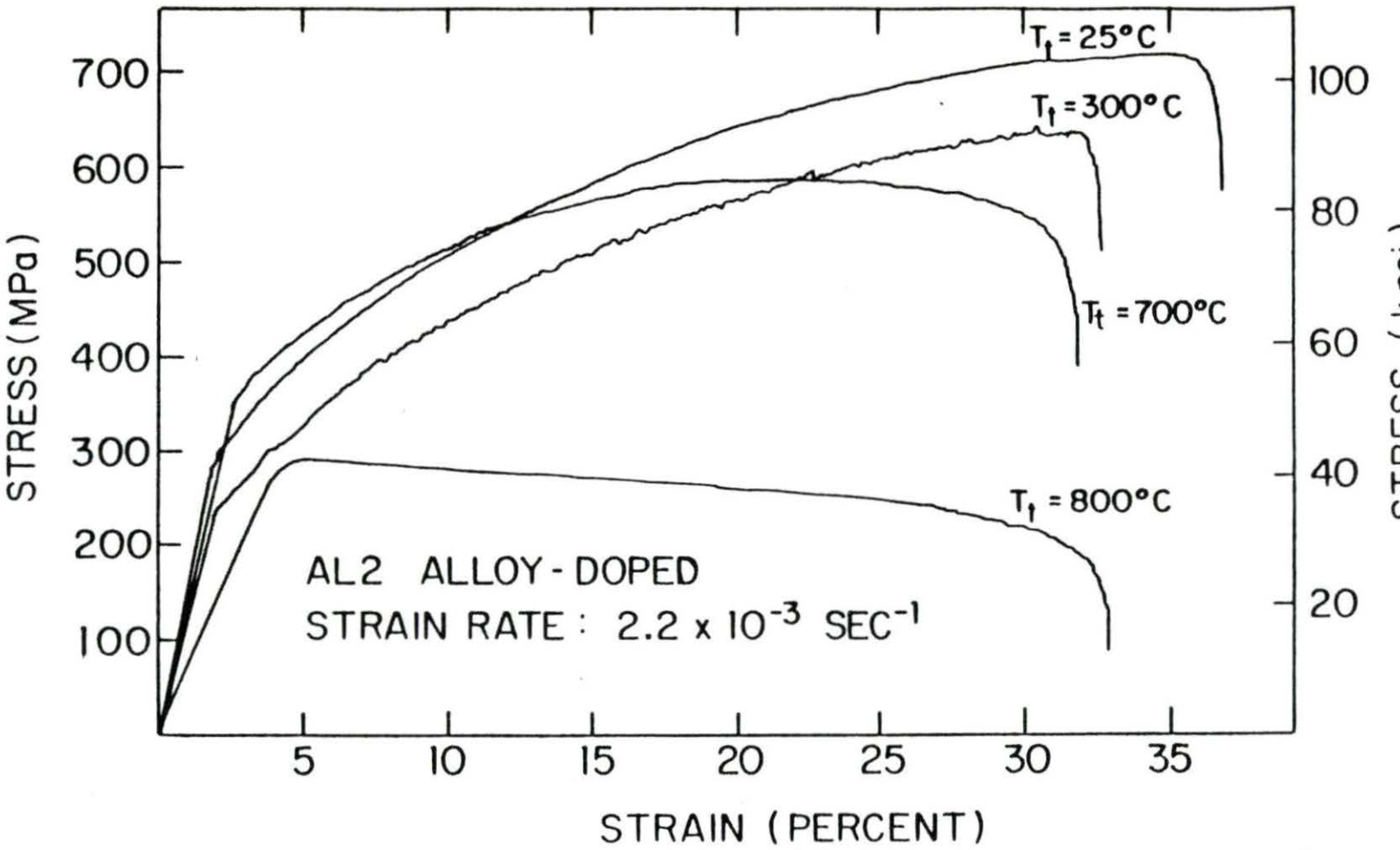

Figure 26. Stress versus strain for doped AL2 alloy tested at 25, 300, 700, and 800 C at strain rate of 2.2 x 10^{-3} sec^{-1}.

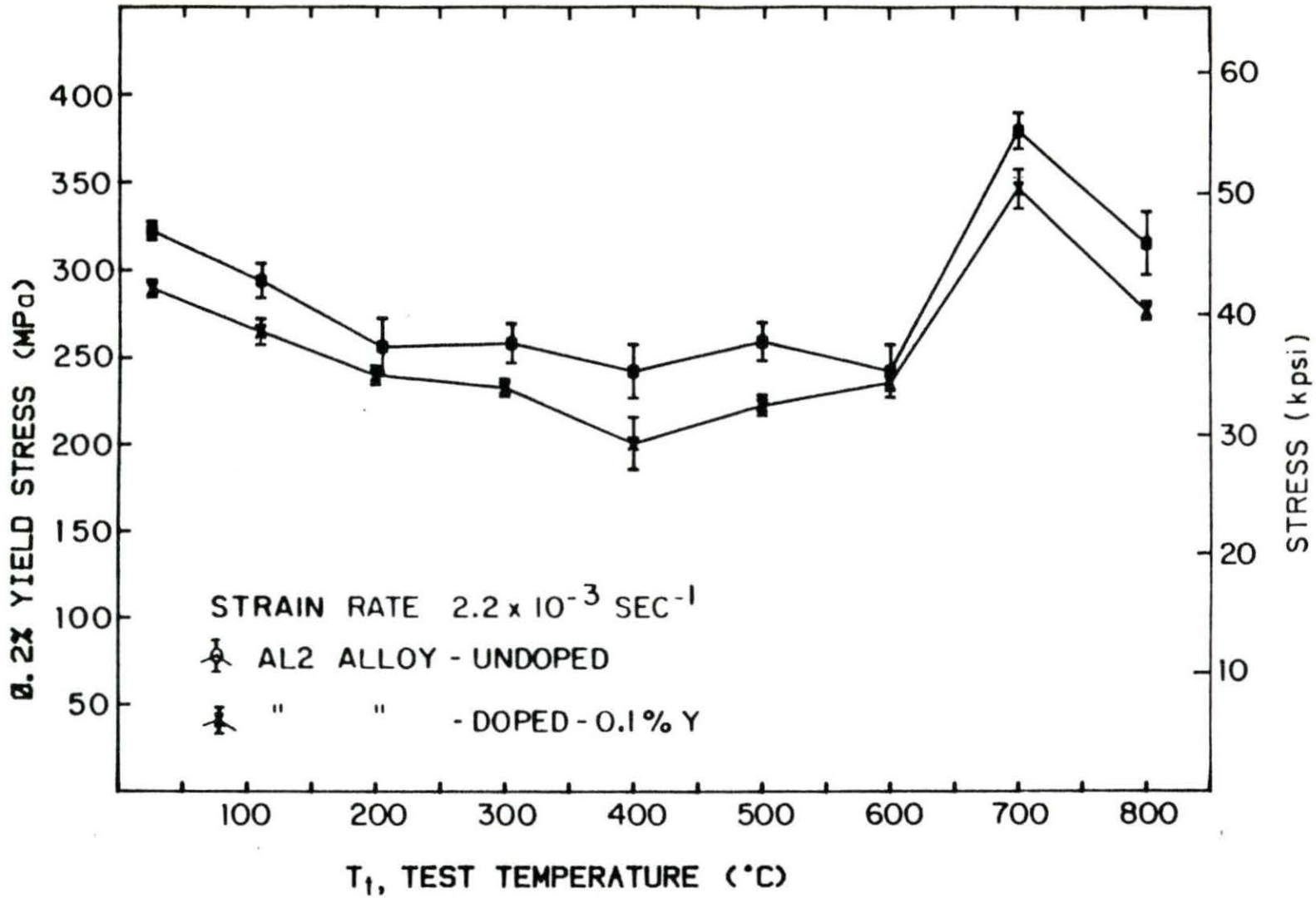

Figure 27. 0.2 percent yield stress of undoped and doped AL2 alloy as a function of test temperature for the strain rate of $2.2 \times 10^{-3} sec^{-1}$.

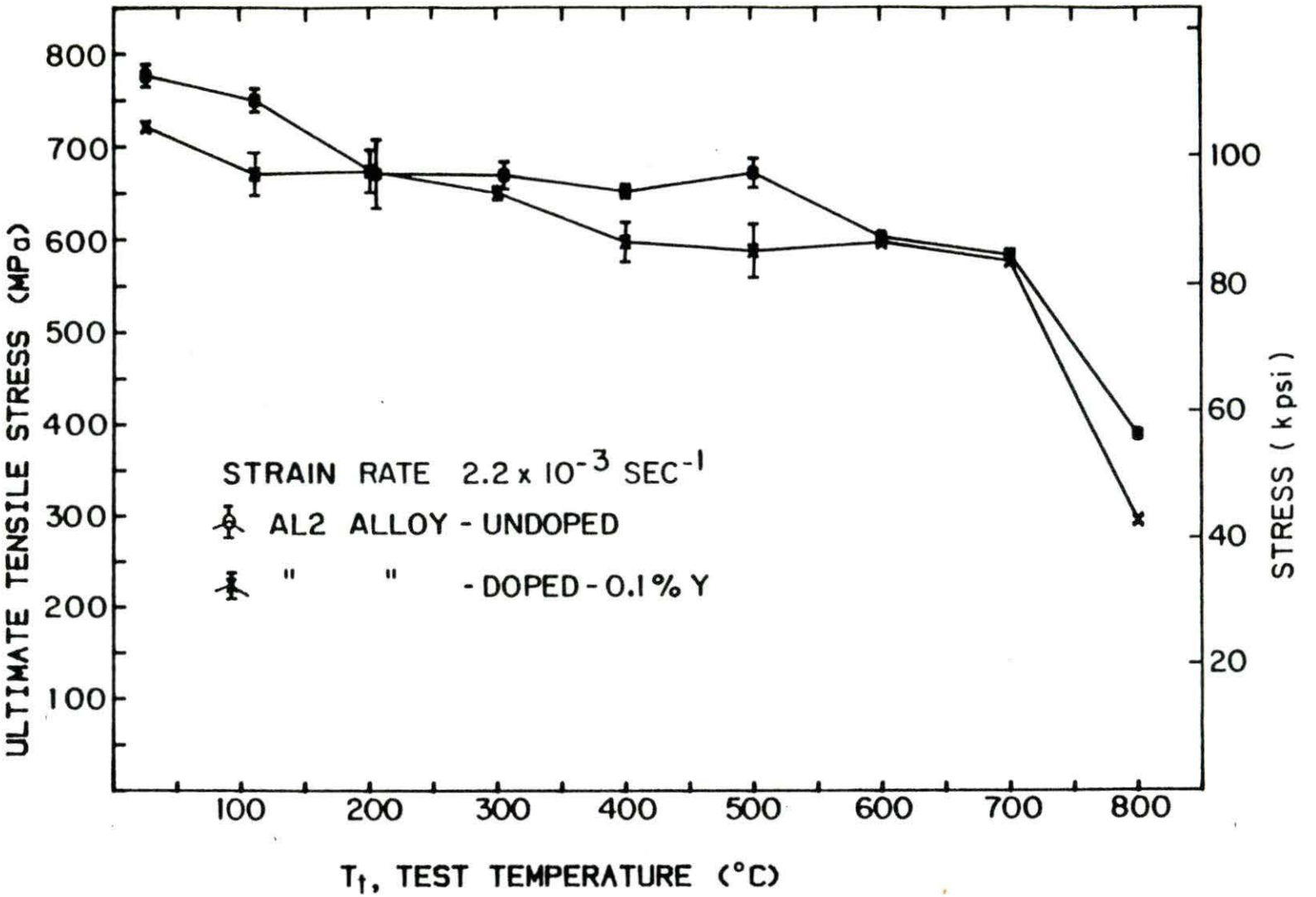

Figure 28. Ultimate tensile stress of undoped and doped AL2 alloy as a function of test temperature for the strain rate of $2.2 \times 10^{-3} sec^{-1}$.

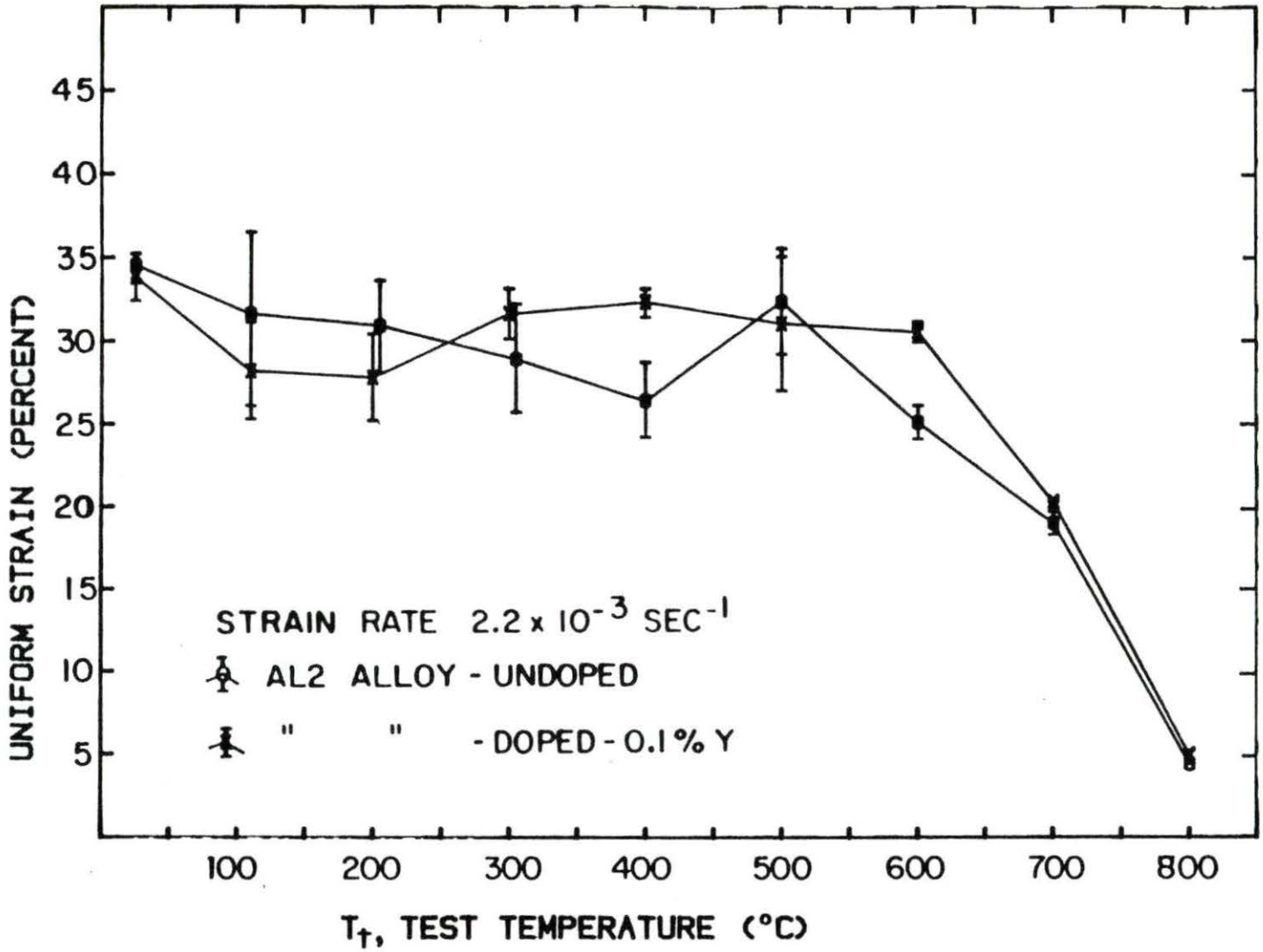

Figure 29. Uniform strain of undoped and doped AL2 alloy as a function of test temperature for the strain rate of $2.2 \times 10^{-3} sec^{-1}$.

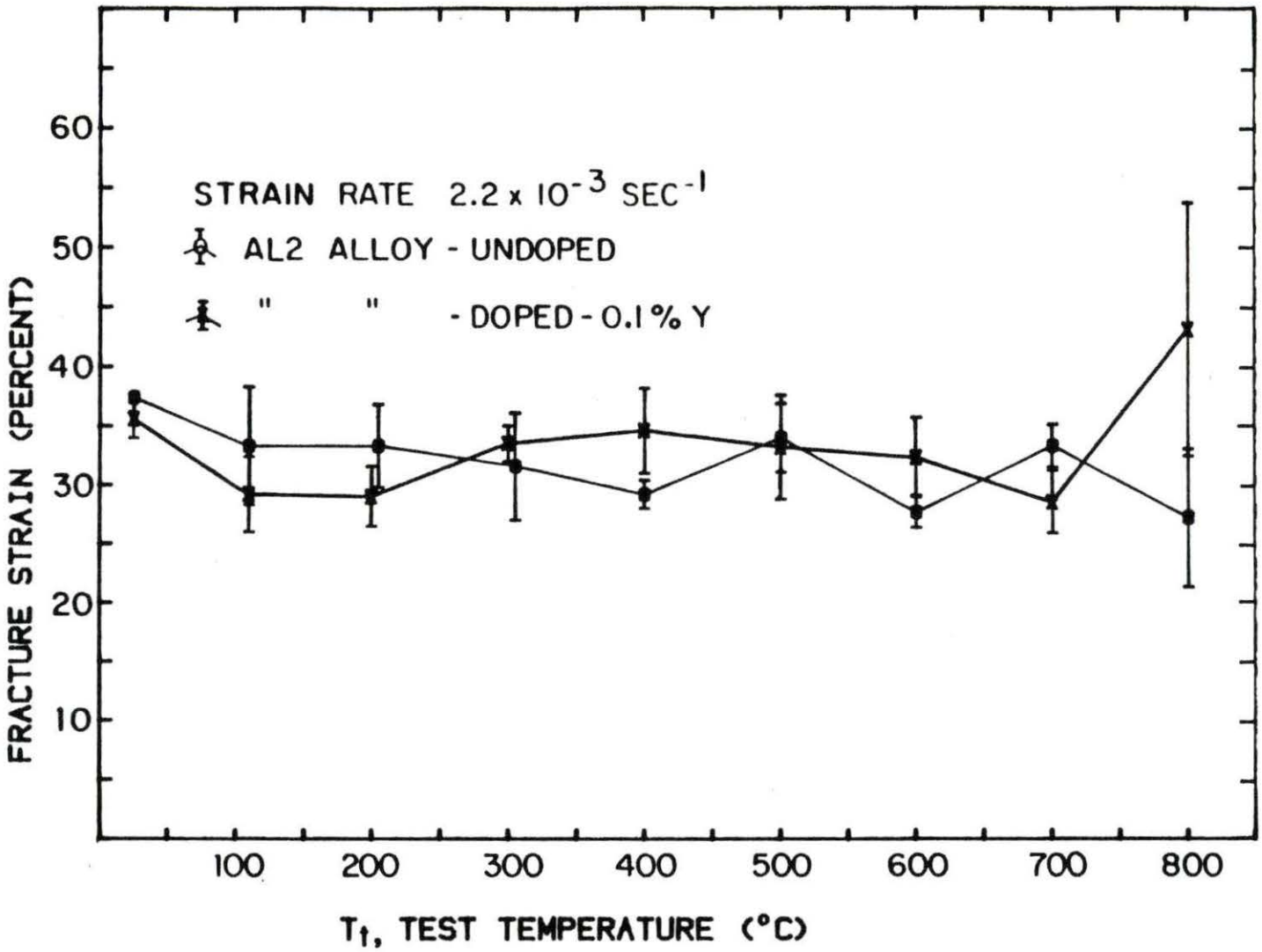

Figure 30. Fracture strain of undoped and doped AL2 alloy as a function of test temperature for the strain rate of $2.2 \times 10^{-3} sec^{-1}$.

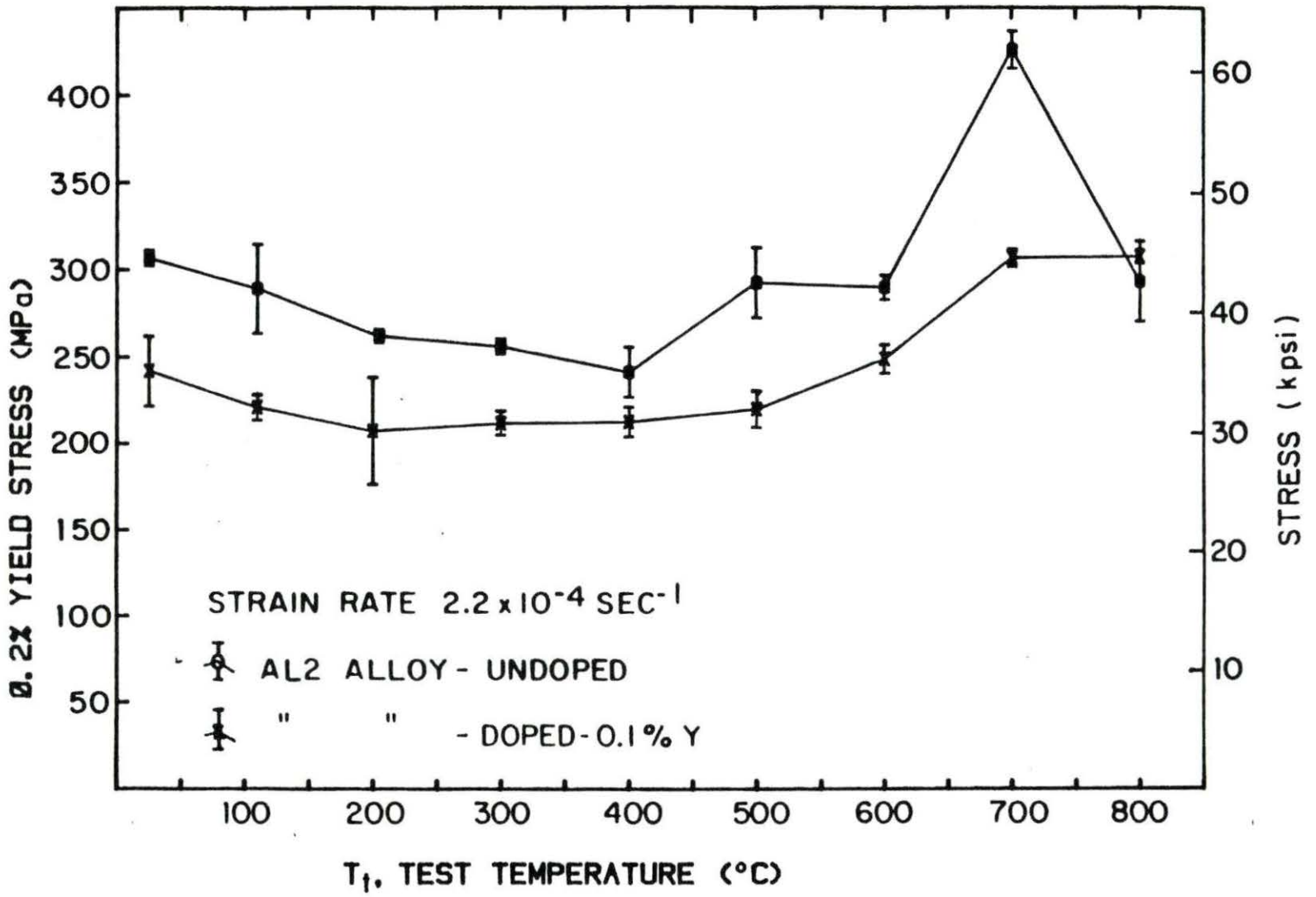

Figure 31. 0.2 percent yield stress of undoped and doped AL2 alloy as a function of test temperature for the strain rate of $2.2 \times 10^{-4} sec^{-1}$.

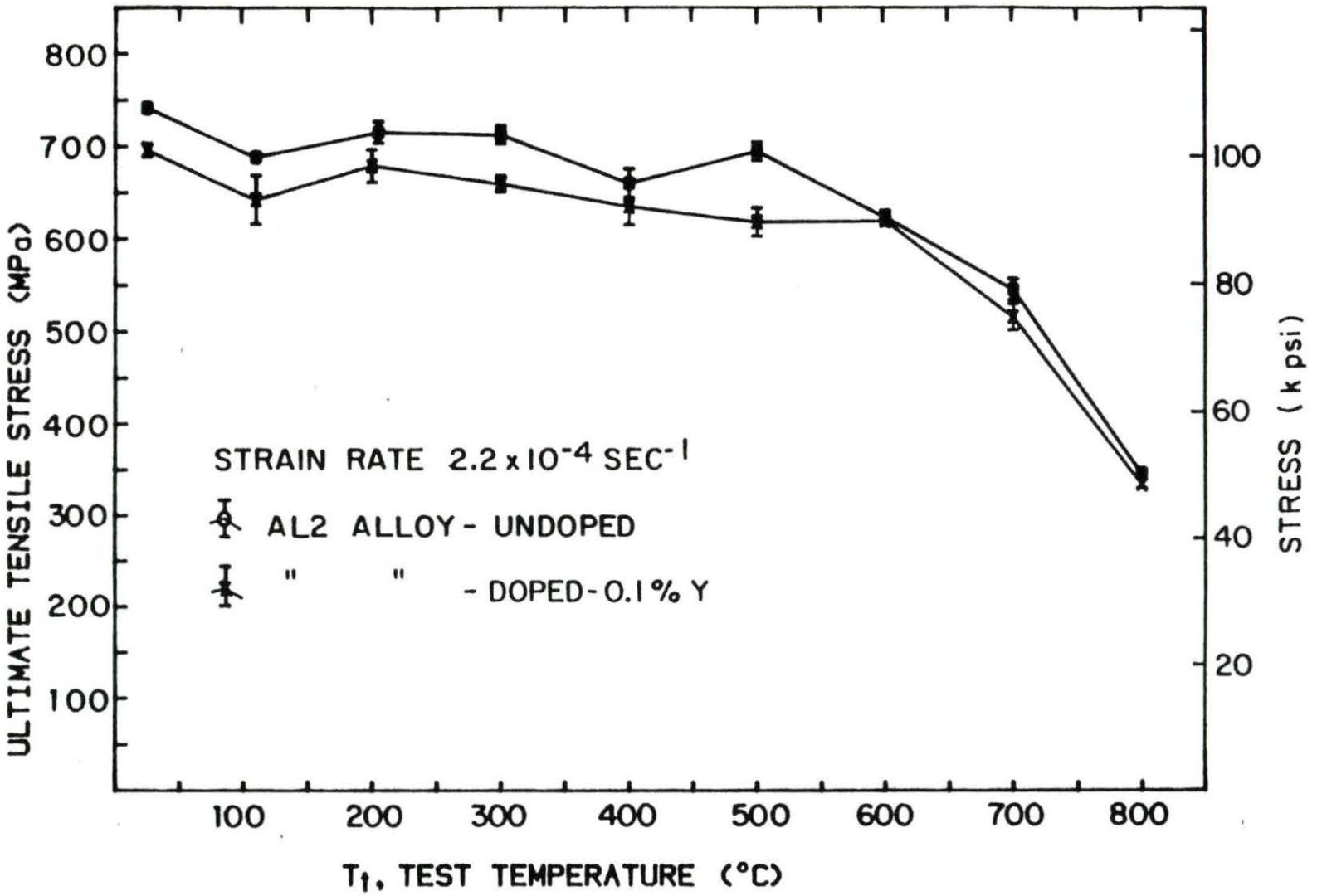

Figure 32. Ultimate tensile stress of undoped and doped AL2 alloy as a function of test temperature for the strain rate of $2.2 \times 10^{-4} sec^{-1}$.

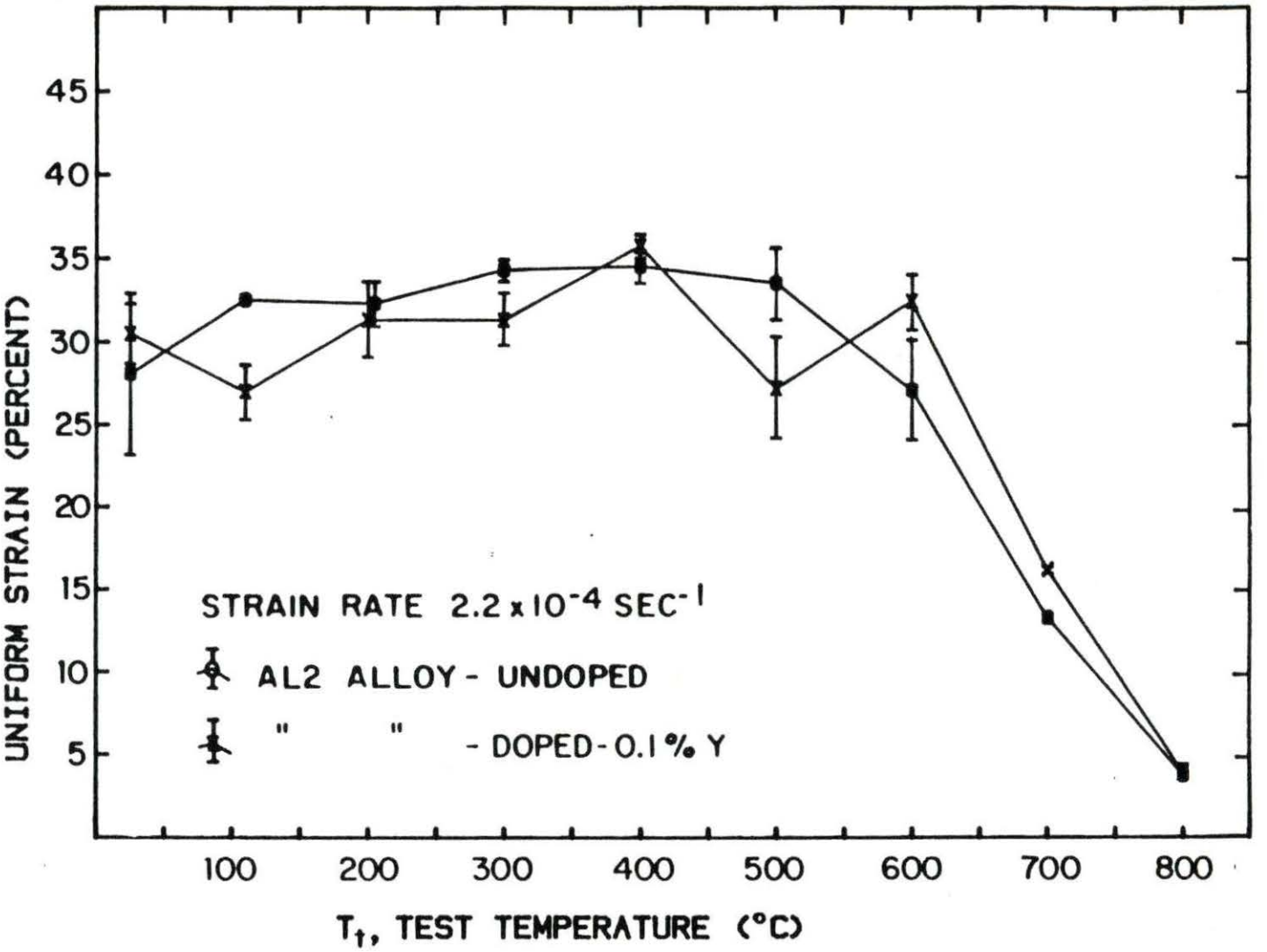

Figure 33. Uniform strain of undoped and doped AL2 alloy as a function of test temperature for the strain rate of $2.2 \times 10^{-4} sec^{-1}$.

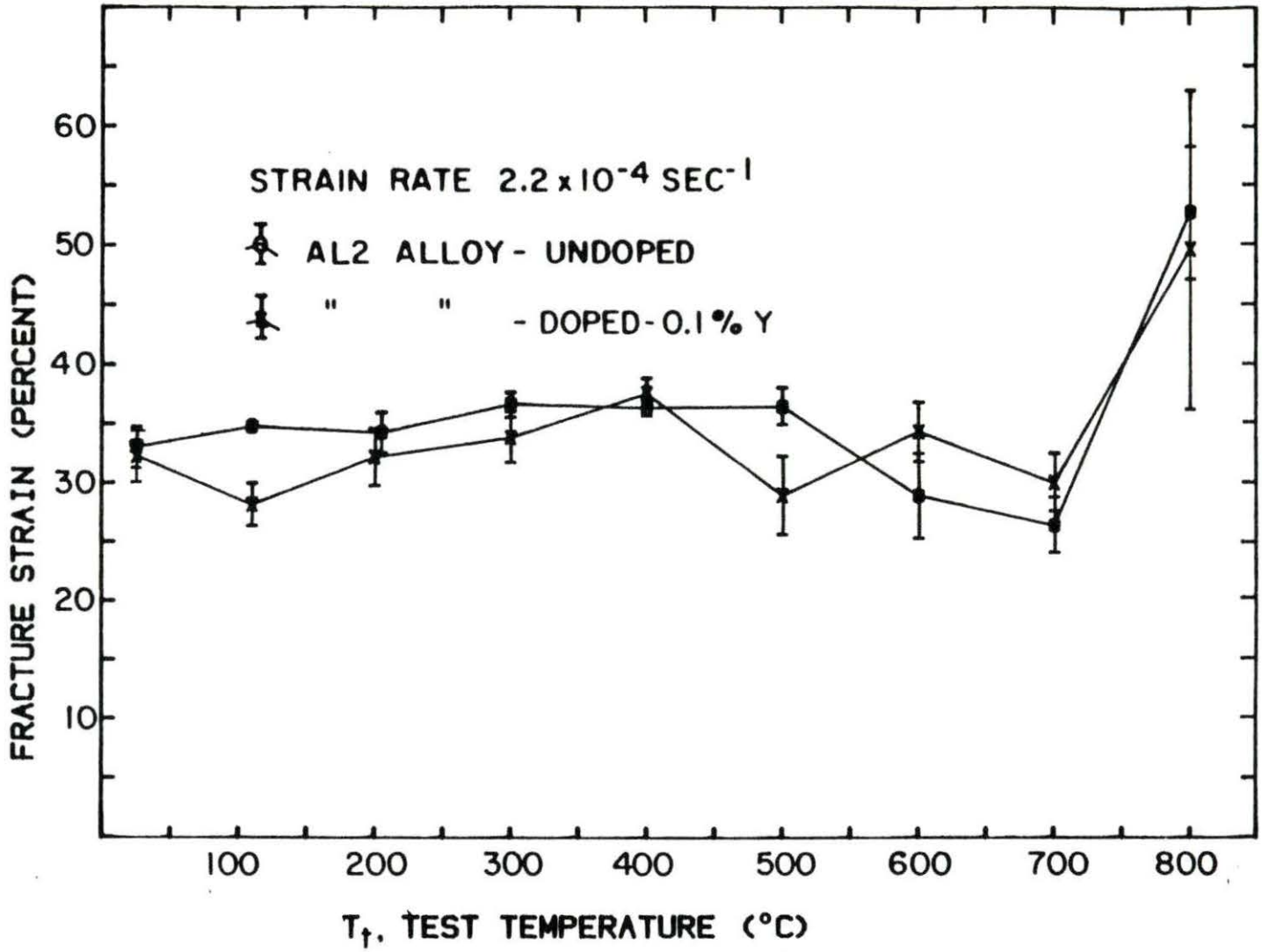

Figure 34. Fracture strain of undoped and doped AL2 alloy as a function of test temperature for the strain rate of $2.2 \times 10^{-4} sec^{-1}$.

and fracture strain (Figures 30 and 34), except possibly a slight increase in these ductility parameters above 600°C.

For both undoped and doped AL2 alloy, dynamic strain aging (serrated yielding or jerky flow) occurred at somewhat elevated temperatures. For strain rate of $2.2 \times 10^{-3}sec^{-1}$, dynamic strain aging was observed at 300 to 600°C (see curve for 305°C in Figure 21), and for $2.2 \times 10^{-4}sec^{-1}$, at 200 to 600°C (see curve for 300°C in Figure 26). In these temperature ranges, detailed shapes of the serrations in the load-time curves changed with temperature. For the strain rate of $2.2 \times 10^{-3}sec^{-1}$, the serrations were coarse at 300-500°C, but they changed to sharp jerky serrations (abrupt rise and drop) at 600°C. For the $2.2 \times 10^{-4}sec^{-1}$ strain rate, the coarse pattern was observed at 200 and 300°C and the jerky one at 400 to 600°C. The two types of patterns are illustrated in Figure 35, where (a) shows coarse serrations and (b), (c), and (c) show jerky ones. Immediately upon yielding, the serrations had small amplitude, but the amplitudes increased with increasing strain and remained constant at high strains (see Figure 35 (c), for example). Specimens tested at 600°C at the lower strain rate showed several groups of jerky serrations linked by smooth lines (see Figure 35 (d)). No difference was observed between the dynamic strain aging behaviors of undoped and doped samples.

C. Hardness Tests

The room temperature and elevated temperature hardness (DPH) measured in the experiments are listed in Table 14 with test temperature for both the doped and undoped AL2 alloy. Figure 36 shows the temperature dependence of hardness (DPH) of the undoped and doped AL2 alloy. Room

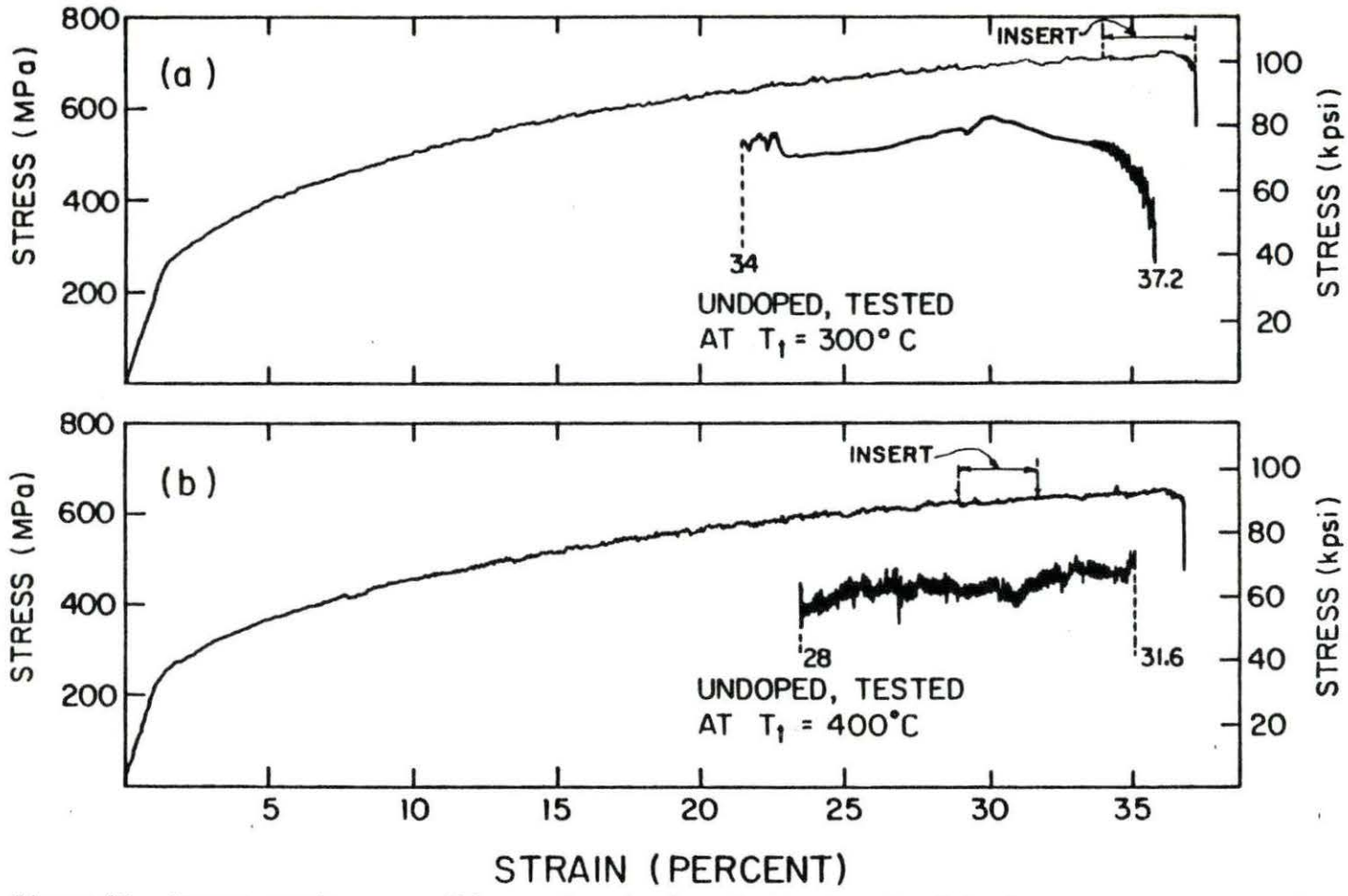

Figure 35. Stress-strain curves illustrating the dynamic strain aging behavior occurred on undoped AL2 alloy specimens for the strain rate of $2.2 \times 10^{-4} sec^{-1} sec^{-1}$. (a) coarse serrations at T_t= 300 C, (b), (c), and (d) jerky serrations at T_t= 400, 500, and 600 C, respectively.

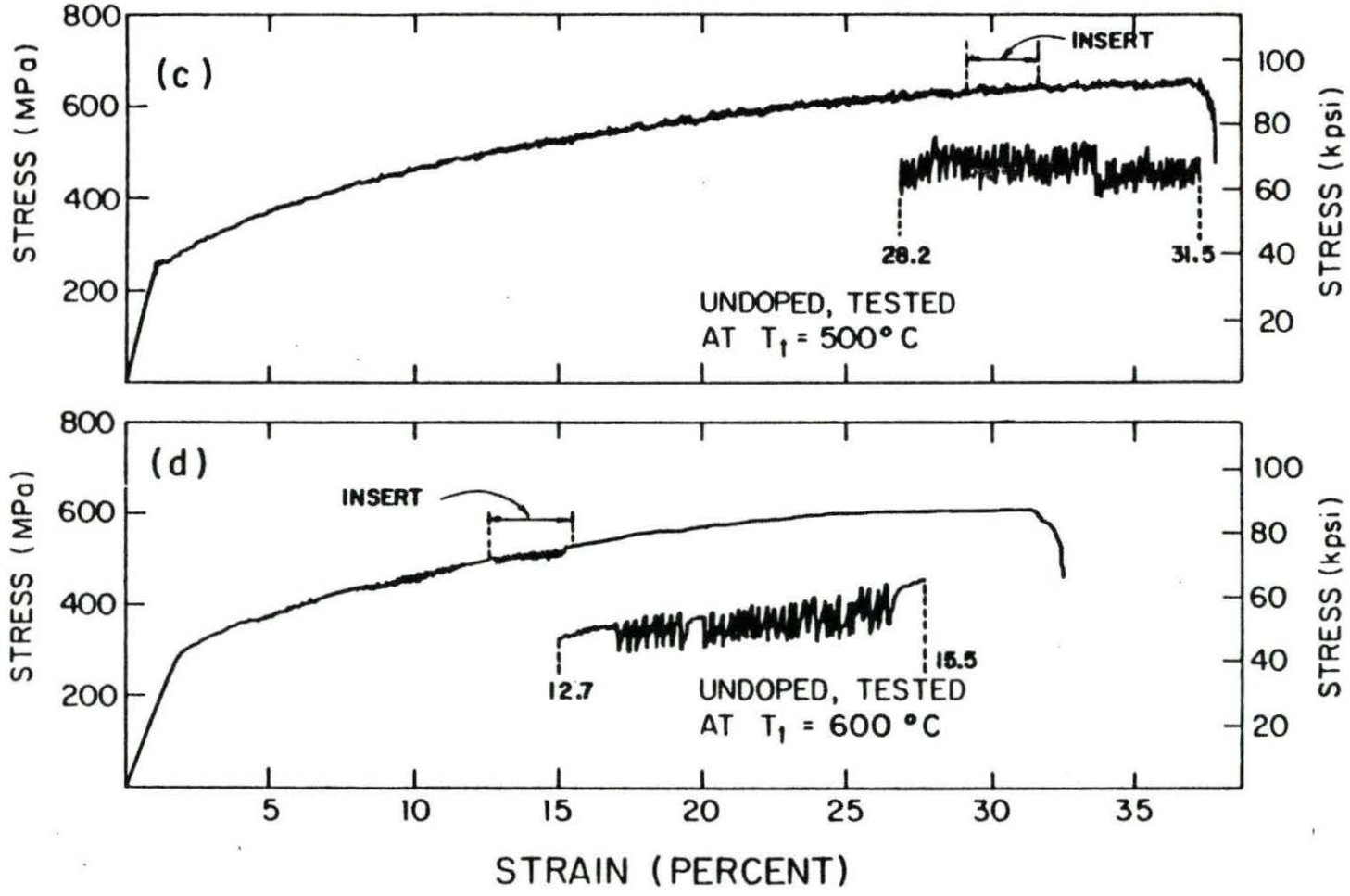

Figure 35 (continued).

Table 14. Results of room temperature and elevated temperature hardness tests for undoped and doped AL2 alloy

Test temperature T_t (^{o}C)	Hardness (DPH)	
	Undoped	Doped
25	207.5 ± 3.2	186.1 ± 6.9
60	200.3 ± 3.0	190.8 ± 5.3
105	197.0 ± 2.8	185.4 ± 2.9
150	189.6 ± 3.9	173.3 ± 3.7
205	184.3 ± 4.0	170.9 ± 4.0
250	178.6 ± 3.8	169.1 ± 1.8
300	178.3 ± 4.5	161.0 ± 5.2
350	173.7 ± 4.2	170.5 ± 3.0
400	166.3 ± 3.1	160.2 ± 2.5
450	163.8 ± 4.5	155.7 ± 3.4
500	160.1 ± 4.7	153.1 ± 3.1
550	153.8 ± 4.3	155.4 ± 5.2
600	159.2 ± 2.4	153.5 ± 3.3
650	149.4 ± 4.0	153.4 ± 1.8
700	152.8 ± 3.3	151.0 ± 2.7
750	160.2 ± 5.9	143.3 ± 2.7
800	175.9 ± 3.7	167.6 ± 4.9
850	168.2 ± 2.8	163.3 ± 3.7

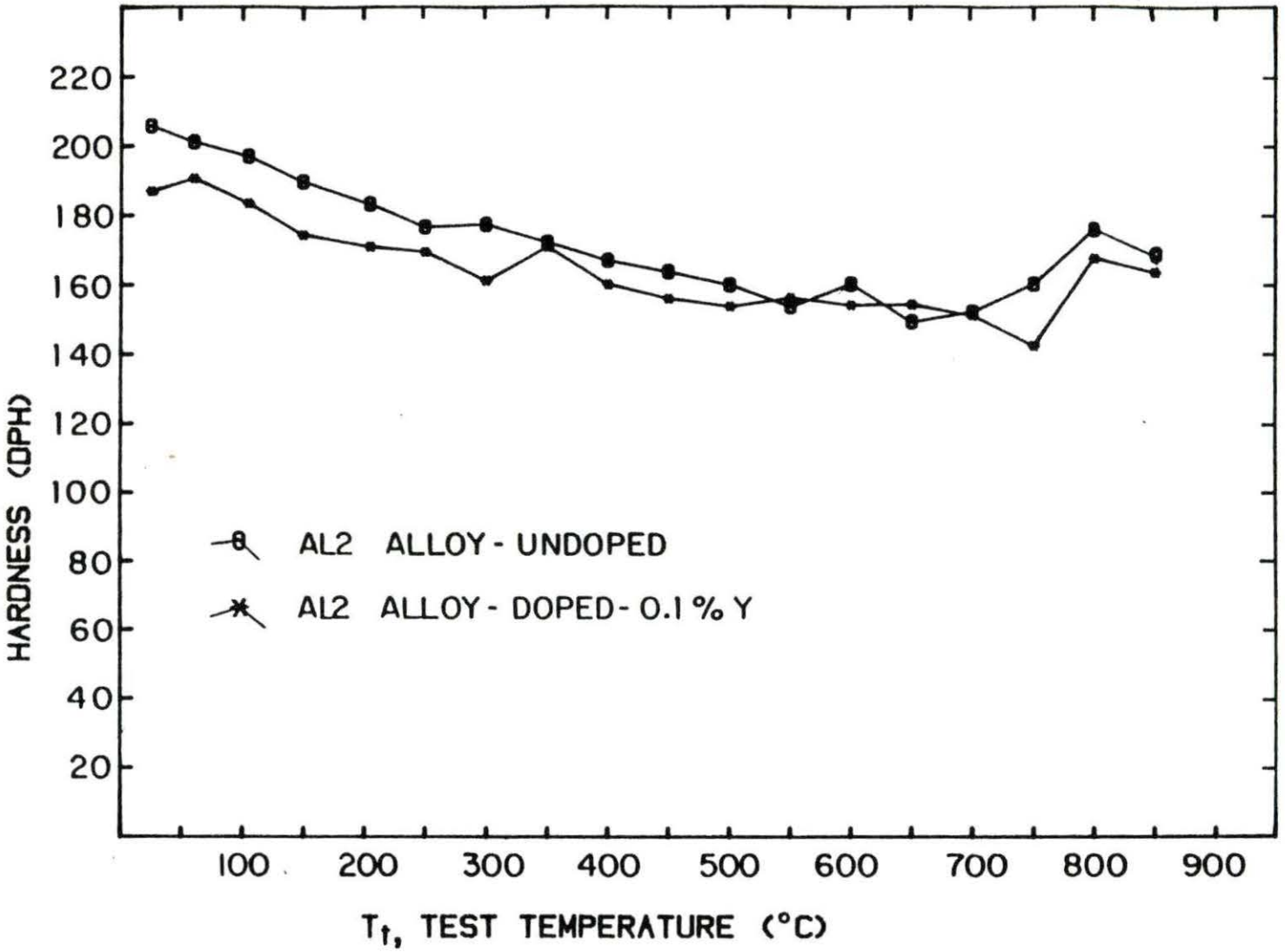

Figure 36. Temperature dependence of hardness of undoped and doped AL2 alloy. Load = 1.2 kg, load application time = 15 sec.

temperature hardness values measured on the cold-rolled and annealed specimens were 207.5 and 186.1 DPH for the undoped and doped specimen, respectively. Hardness measured at elevated temperature on the undoped AL2 alloy specimen showed a gradual decrease with increasing temperature up to 650°C, followed by an increase. The minimum hardness was found to be 149.4 DPH at 650°C. Above 650°C, DPH increased, but did not suggest further increase with increasing temperature. For the doped alloy, as is in the undoped alloy, the hardness dropped gradually to the value of 153.1 DPH at 500°C. In the temperature ranges from 250 to 700°C, the hardness of the doped alloy did not change much, indicating insensitivity to the temperature. Measured minimum DPH was found to be 143.3 at 750 °C. From 750°C, DPH increased in a rapid way, but the hardness measured at 850°C did not show the further increase in DPH above 850°C.

Yttrium addition of 0.1 wt % did not improve the hardness of AL2 alloy in the entire test temperature range employed. Average reductions in hardness over the test temperature ranges were found to be ∿5% by 0.1 wt % yttrium addition.

IV. DISCUSSION

The results of the current investigations on the effect of 0.1% yttrium addition on the high temperature tensile properties and hardness of Fe-34% Ni - 12% Cr Al2 alloy indicate the decrease in yield stress, ultimate tensile stress and hardness of the alloy over the entire range of test temperatures, although small increases in ductility at temperatures of 600°C and above were shown. The yttrium addition did not change the general trends of the temperature dependence of yield stress, ultimate tensile stress and hardness of the base alloy, but it reduced the strength and hardness by moderate amounts over the entire range of test temperatures (room temperature to 850°C).

The decreases in yield stress in the low temperature ranges (below 200 or 300°C) might be due to the increasing ease of movement of dislocations with increasing temperature because of the weakening of impeding barriers presented in the matrix. In the temperature ranges where the dynamic strain aging occurred, yield stress and ultimate stress showed little dependence on test temperature. Dynamic strain aging may be associated with the interaction between the impurity solute atoms and dislocations during deformation, and it has a close relationship with tensile properties (56,57). With increasing the strain rate from $2.2 \times 10^{-4} sec^{-1}$ to $2.2 \times 10^{-3} sec^{-1}$, the lower temperature limit where dynamic strain aging was observed increased from 200°C to 300°C. In this temperature range, yield stress was found to be almost independent of temperature. Flow stress was found to be almost independent of strain rates. Generally speaking, ductility parameters are also found to be somewhat independent

of temperature. Work hardening rate was found to be almost independent of temperature and to be exceptionally high compared to values at higher test temperature where dynamic strain aging did not occur.

In the temperature ranges where dynamic strain aging occurred, hardness also showed almost independence to the test temperature. At high temperature (Tt > 600^{o}C), a peak occurred in yield stress versus temperature and also the hardness increased. These observations suggest a hardening reaction occurred in this temperature range.

As is shown in Figure 37, the free energies of formation of yttrium nitride, oxide, carbide, and sulfide are far lower than for the corresponding iron compounds. The yttrium compounds, if they are present as precipitates in the matrix, might inhibit the dislocation movement during plastic deformation and would be expected to increase the yield and ultimate tensile stresses (precipitation hardening). However, no such strengthening was observed. Therefore, it appears that the above-mentioned compounds did not precipitate out within the grains.

On the other hand, early reports indicated improvement in hot plasticity, deformability, ductility and workability of steels by REM additions (40-43). These beneficial effects can be also attributed to the elimination of non-metallic inclusions from the grain boundaries by REMs and corresponding improvement in grain boundary properties.

Reports by Pridantsev and Ostapenko (41) stated that negative effects of REM addition have a relationship with nitrogen contents in the steel. They indicated that smaller additions than optimal amounts have no effect on deformability in the heated conditions, while larger amounts lead to

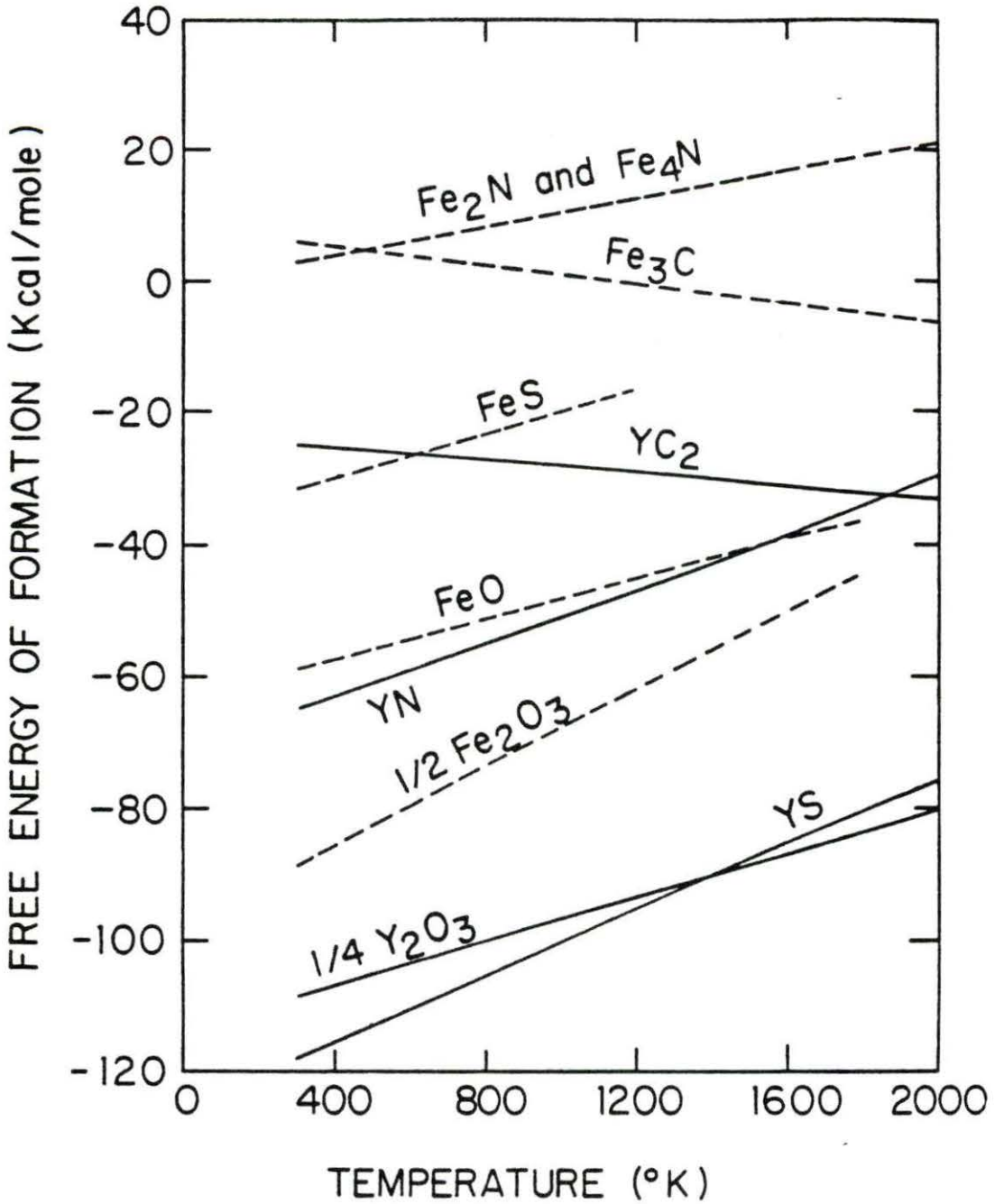

Figure 37. Free energies of formation for iron and yttrium carbides, nitrides, sulfides and oxides as a function of temperature (from Ref. 34)

negative effects. It was also reported that yttrium addition is less effective in nitrogen-containing steels probably due to the formation of hard and brittle yttrium nitride (42). In connection with nitrogen and ductility of steels, the optimum amounts of yttrium addition for austenitic steel are known to be affected by nitrogen content in the steel.

In the study of austenitic chromium-nickel steel, V. K. Farafonov et al. (36) found that amount and size of nonmetallic inclusions in steel increases with increasing yttrium content. They also indicated that rare earth metal addition does not change the grain size of austenitic chromium-nickel steel and nickel-base alloy.

Reviewing the results of electron microprobe work performed on the homogenize-annealed and cold-rolled 60-mil sheets, the high concentration of Nb and Ti in the inclusions within the grain suggests this phase to be Ni_3Ti and Ni_3Nb. The conversion of Ni_3Ti to Ni_3Nb was reported (58). Also, grain boundary precipitates are supposed to be Ni_3Ti and Ni_3Nb. In this sense, the major strengthening phase in the AL2 alloy is supposed to be Ni_3Ti and Ni_3Nb. High concentrations of yttrium at the grain boundary inclusions and inclusions within the grains suggest a depletion of yttrium and impurity solute atoms from solid solution, reducing the hardening actions of impurity solute atoms within grains.

In their study on the Fe-15% Cr-4% AL alloy for the application of this alloy as fuel cladding in high temperature CO_2-cooled reactors, A. C. Roberts et al. (59) reported that 0.86% yttrium additions reduce the grain coarsening tendencies and, at the same time, remove high-temperature embrittlement. They also reported the improvement in post-irradiation

yield stress and ultimate tensile stress by 0.86% yttrium addition. Associated with the YFe_9 precipitates, improvement in post-irradiation ductility was reported as a result of the retention of boron and helium within the grains and away from the boundaries. According to a recent study by R. D. Hopson (44) on the effect of yttrium addition on the void swelling of AL2 alloy using 4 MeV $^{56}Fe^{2+}$ ion bombardment, peak swelling of undoped AL2 alloy decreased as much as 20% by 0.1% yttrium addition.

The results of the current study and the above-mentioned two investigations indicate the need for more extensive research on the effect of yttrium additions on the properties of the AL2 alloy. Of particular importance is the determination of the optimum yttrium concentrations with respect to the strength, ductility, and radiation stability of the alloy.

V. SUMMARY

The effect of the addition of yttrium on the elevated temperature tensile properties and hardness of an Fe-34% Ni-12% Cr candidate LMFBR cladding and duct alloy was investigated. Tensile tests were performed from room temperature to 800°C in 100°C steps at strain rates of 2.2×10^{-3} and $2.2 \times 10^{-4} sec^{-1}$. Hardness tests were performed from room temperature to 850°C in 50°C steps.

The addition of 0.1% yttrium decreased the yield stress and ultimate tensile stress in the test temperature range employed. Hardness also decreased over this test temperature range. In tensile tests, dynamic strain aging behavior occurred both for the undoped and doped alloy in the temperature range from 200 to 600°C and 300 to 600°C for the lower and higher strain rate, respectively.

Electron microprobe performed on cold rolled specimens showed yttrium concentrations in the matrix lower than the bulk concentration, while showing twice the bulk concentration at grain boundary inclusions. The decrease in yield and tensile strength and hardness by yttrium addition is attributed to the removal of impurity solute atoms by yttrium from the matrix, reducing the hardening actions of impurity solute atoms within the grains.

VI. REFERENCES

1. J. W. Bennett and K. E. Horton, Materials requirements for liquid metal fast breeder reactors, Met. Trans. 9A, 143 (1978).

2. Kurt Goldmann, Liquid sodium as a reactor coolant, in National Topical Meeting on Fast Reactor Systems, Materials and Components, edited by W. E. Niemuth and J. F. Weissenberg, CONF-680419, U.S. Atomic Energy Commission, Washington, D.C., 244 (1968).

3. Karl Wirtz, Lectures on Fast Reactors/Karl Wirtz-Karlsruhe Germany; Gesellshaft für Kernforschungszentrum, c1973.

4. A. J. Friedland, Coolant properties, heat transfer, and fluid flow of liquid metals, Chap. 2 in Fast Reactor Technology: Plant Design, edited by John G. Yevick and A. Amorosi, the MIT Press, Cambridge, Mass., 1966.

5. D. H. Gurinsky, Some materials problems in fast reactors, in National Topical Meeting on Fast Reactor Systems, Materials and Components, edited by W. E. Niemuth and J. F. Weissenberg, CONF-680419, U.S. Atomic Energy Commission, Washington, D.C., (1968).

6. R. L. Klueh and J. H. DeVan, Vanadium alloy development for sodium cooled reactors, Nucl. Eng. and Des. 17, 371 (1971).

7. G. P. Scheidler, M. J.Makin, F. J. Minter and W. F. Schilling, The effect of irradiation temperature on the formation of clusters in neutron irradiated copper, in The Nature of Small Defect Clusters; AERE-R5269, Atomic Energy Research Establishment, Harwell, England, (1966).

8. J. L. Brimhall, H. E. Kissinger, and G. L. Kulcinski, The effect of temperature on void formation in irradiated pure and impure metals, in Radiation-Induced Voids in Metals, U.S. Atomic Energy Commission, Washington, (1972).

9. T. T. Claudson, Agenda discussion, in Irradiation Effects on Structural Alloys for Nuclear Applciations, ASTM, STP 484, American Society for Testing and Materials, Philadelphia, PA, (1970).

10. J. J. Holmes and J. L. Straalsund, Effect of cold work on irradiation-induced swelling, Trans. Amer. Nucl. Soc. 13, 559 (1970).

11. E. E. Bloom, Nucleation and growth of voids in stainless steels during fast-neutron irradiation, in Radiation Induced Voids in Metals, U. S. Atomic Energy Commission, Washington, 1 (1972).

12. W. G. Johnston, J. W. Rosolowski, A. M. Turkalo and T. Lauritzen, An experimental survey of swelling in commercial Fe-Cr-Ni alloys bombarded with 5 MeV Ni ions, J. Nucl. Mater. 54, 24 (1974).

13. W. G. Johnston, T. Lauritzen, J. H. Rosolowski and A. M. Turkalo, Void swelling in fast reactor materials - a metallurgical problem, J. Metals 28, 19 (1976).

14. E. H. Lee and A. F. Rowcliffe, The effect of compositional modifications on the low temperature swelling in D9 type alloys, in National Cladding/Duct Materials Development Program, Annual Information Meeting TC-1978 (addendum 1), Hanford Engineering Development Laboratory, Richland, Washington, (1980).

15. G. R. Gessel, Effects of minor alloying additions on the strength and swelling behavior of an austenitic stainless steel, ORNL/TM6359, Oak Ridge National Laboratory, Oak Ridge, Tennessee, 1978.

16. M. L. Bleiberg and J. W. Bennett, eds. International Conference; Radiation Effects in Breeder Reactor Structural Materials, The Metallurgical Society of AIME, New York, 1977.

17. J. R. Weir, J. O. Stiegler, and E. E. Bloom, Irradiation behavior of cladding and structural materials, in Proceedings of the National Topical Meeting on Fast Reactor Systems, Materials and Components, CONF-680419, U.S. Atomic Energy Commission, Washington, (1968).

18. W. R. Martin and J. R. Weir, Effect of irradiation temperature on the post irradiation stress-strain behavior of stainless steel, in Flow and Fracture of Metals and Alloys in Nuclear Environments, STP 380, American Society for Testing and Materials, Philadelphia, PA, (1965).

19. E. E. Bloom, W. R. Martin, J. O. Stiegler, and J. R. Weir, The effect of irradiation temperature on the strength and microstructure of stainless steel, J. Nucl. Mater. 22, 68 (1967).

20. F. R. Shober and W. E. Murr, Radiation induced property changes in AISI type 347 stainless, in Symposium on Radiation Effects on Metals and Neutron Dosimetry, STP 341, American Society for Testing and Materials, Philadelphia, PA, (1963).

21. E. E. Bloom, In-reactor and post-irradiation creep-rupture properties of type 304 stainless steel at 650°C, ORNL/TM-2130, Oak Ridge National Laboratory, Oak Ridge, Tenn., 1968.

22. W. R. Martin and J. R. Weir, Solutions to the problems of high-temperature irradiation embrittlement, STP 426, American Society for Testing and Materials, Philadelphia, PA, (1967).

23. R. A. Mintern, New uses for the rare earths, New Scientist 14, 225 (1962).

24. V. F. Terekhova and E. M. Savitskii, Yttrium, Israel Program for Scientific Translations, Jerusalem, 1970.

25. W. Kermet Anderson, Nuclear applications of yttrium and the lanthanons, Chapt. 12, in The Rare Earths, edited by F. H. Spedding and A. H. Daane, John Wiley & Sons, Inc., New York and London, (1961).

26. J. R. DiStefano, Compatibility of Eu_2O_3 with Type 316 Stainless Steel and Sodium, ORNL/TM-4780, Oak Ridge National Laboratory, Oak Ridge Tenn., 1975.

27. Taylor Lyman et al., editors, Properties and selection, in Metals Hand Book, 8th edition, Vol. 1, American Society for Metals, Metals Park, Ohio, 1970.

28. M. D. Goldberg, S. F. Mughabghab, B. A. Magurno, and V. M. May, editors, Neutron Cross Sections, BNL 325, IIA, Z=21-40, Second edition, Supplement No. 2, Brookhaven National Laboratory, Upton, New York, 1966.

29. Gerhard Kirschstein, Dieter Koschel and Joachim Wagner, editors, Gmelin Handbuch der Anorganischen Chemie, Springer-Verlag, Berlin, Heidelberg, New York, (1976).

30. J. F. Francis, Structure of the surface oxides formed on a 20% Cr/25% Ni/Nb-stabilized steel in carbon dioxide at high temperatures, Br. Corros. J. 3, 113 (1968).

31. J. M. Francis and W. H. Whitlow, High temperature oxidation resistance of an yttrium bearing 20% Cr/25% Ni/Nb-stabilized austenitic steel in carbon dioxide, J. Iron and Steel Inst. 204, 355 (1966).

32. J. E. Antill and K. A. Peakall, Influence of an alloy addition of yttrium on the oxidation behavior of an austenitic and a ferritic stainless steel in carbon dioxide, J. Iron and Steel Inst. 205, 1136 (1967).

33. J. M. Francis, J. A. Jutson, High temperature oxidation studies of rare earth metal addition to an austenitic stainless steel, J. Iron and Steel Insti., 207, 639 (1969).

34. N. Kippenhan and K. A. Gschneidner, Jr., Rare-earth metals in steels, Report IS-RIC-4, Rare-Earth Information Center, Iowa State University, Ames, Iowa, 1970.

35. A. Raman, Uses of rare earth metals and alloys in metallurgy, Zeitschrift für Metallkunde 67 (11), 780 (1976).

36. V. K. Farafanov, M. M. Shteinberg, Z. G. Fret'yakova, and V. V. Voinov, Influence of rare-earth metals on the properties of austenitic chromium-nickel steel, Metalloved. Term. Obrabot. Metal. 4, 50 (1967)

37. A. G. Gryaznov and I. V. Paisov, The effect of rare earth metals on the hot ductility of Cr-Ni Mo steel, Vest. Mashinostr. 45, No. 11, (1965)1 Eng. Trans.-Russ. Eng. J. 45, No. 11, 65 (1965).

38. A. G. Gryaznov and I. V. Paisov, Improving the structure and properties of austenitic steel by adding rare earth metals, Vest. Mashinostr. 46, No. 7, 69 (1966); Eng. Trans.-Russ. Eng. J. 46, No. 7, 69 (1966).

39. P. D. Parsons, Yttrium to give steel protection, New Scientist, 32, 516 (1966).

40. L. S. Etelis, M. I. Gladkov, D. G. Ryabova, and E. N. Kurteyev, The influence of yttrium on the properties of steels 40L and Kh18N9L, Izv. Akad. Nauk. Sssr Metally 1974, No. 6, 172-4; Eng. Trans.-Russ. Met., No. 6, 140 (1974).

41. M. V. Pridantsev, T. V. Ostapenko, Effect of REM on the plasticity of austenitic stainless steels in the heated condition, Met. Term. Obrab. Met. 1974, No. 7, 68-71; Eng. Trans.-Met. Sci. Heat Treat. 16, 618 (1974).

42. Ya. E. Gol'dshtein, S. N. Chuvitina, M. N. Shmatko, and L. V. Sergeeva, Effect of small yttrium additions on the hot plasticity of corrosion resistant steels and an alloy of the austenitic class, Met. Term. Obrab. Met. 1978, No. 6, 20-2; Eng. Trans.-Met. Sci. Heat Treat. 20, 451 (1978).

43. M. P. Braun and Yu. Ya. Skok, Effect of calcium silicide and rare earth metal additions on the ductility of structural steels, Fiz. Khim. Mekhan. Mate., Vol. 2, No. 3, pp. 333-335, 1966; Eng. Trans.-Sov. Materials Sci. 2, 238 (1966).

44. R. D. Hopson, The effect of yttrium additions on void swelling in liquid metal fast breeder reactor candidate cladding alloys, M.S. thesis, Iowa State University, Ames, Iowa, 1981.

45. M. Z. Shah Khan, The effect of yttrium additions on the tensile properties and hardness of an iron-nickel-chromium alloy, M.S. thesis, Iowa State University, Ames, Iowa, 1981.

46. Standard methods of verification of testing machines, ASTM E4-72 in Annual Book of ASTM Standards, American Society for Testing and Materials, Philadelphia, PA, 10, (1974).

47. Standard methods of tension testing of metallic materials, ASTM E8-69 in Annual Book of ASTM Standards, American Society for Testing and Materials, Philadelphia, PA, 10, (1974).

48. Standard recommended practice for elevated temperature tension tests of metallic materials, ASTM #21-70, in Annual Book of ASTM Standards, American Society for Testing and Materials, Philadelphia, PA, 10, (1974).

49. Standard recommended practice for tension tests of metallic materials at elevated temperatures with rapid heating and conventional or rapid strain rates, ASTM E151-64, in Annual Book of ASTM Standards, American Society for Testing and Materials, Philadelphia, PA, 10, (1974).

50. Drawings for Micro Hot-Hardness Tester, Drawings D-5006-1 through D-5006-8, Oak Ridge National Laboratory, Oak Ridge Tenn.

51. F. Garofalo, P. R. Malenock, and G. V. Smith, Hardness of various steels at elevated temperatures, Trans. Amer. Soc. Metals, 45, 377 (1953).

52. E. R. Petty and H. O'Neil, The hardness of iron, low-carbon steels, and cast iron roll materials at various temperatures, J. Iron Steel Inst., 197, 141 (1961).

53. Standard test method for microhardness of materials, ASTM E 384-73 in Annual Book of ASTM Standards, American Society for Testing and Materials, Philadelphia, PA, 10, (1976).

54. Standard method of test for Vicker hardness of metallic materials, ASTM E92-72 in Annual Book of ASTM Standards, American Society for Testing and Materials, Philadelphia, PA, 10, (1974).

55. George E. Dieter, Mechanical Metallurgy, 2nd ed., McGraw-Hill Book Co., 1976.

56. R. E. Reed-Hill, Physical Metallurgy Principles, 2nd Edition, Van Nostrand Co., Inc., New York, 1972.

57. J. D. Baird, Dynamic strain aging, Chapter 8 in The Inhomogeneity of Plastic Deformation, American Society for Metals, Metals Park, Ohio, 1973.

58. R. F. Decker, Strengthening mechanisms in nickel-base superalloys in Steel Strengthening Mechanisms Symposium, Climax Molybdenum Co., Greenwich, Conn., 1970.

59. A. C. Roberts, D. R. Harris, D. R. Arkel, M. P. Dewey, and J. D. H. Hughes, Effects of yttrium on the structure and post-irradiation tensile properties of an iron-chromium-aluminum alloy, in Symposium on Irradiation Effects in Structural Alloys for Thermal and Fast Reactors, STP 451, American Society for Testing and Materials, Philadelphia, PA, (1969).

VII. ACKNOWLEDGEMENTS

I would like to give deep gratitude to Dr. Monroe S. Wechsler for his guidance and suggestions during this research. I also would like to thank Wes Alexander for his willing assistance during this research, and Donna Gladon for typing this thesis. I also appreciate the help of B. L. Evans of Rare Earth Information Center and the technical staff of Ames Laboratory during the course of this investigation, especially H. H. Baker for metallography and F. C. Laabs for electron microprobe work. Thanks also go to J. J. Laidler and J. L. Straalsund of the Hanford Engineering Development Laboratory for providing the starting alloy. Finally, I would like to thank the taxpayer of Korea and the Ministry of Education of the Korean Government for giving me the opportunity and finances to achieve my academic goals.